Chapter 2
Fabrication and Investigation of Intermediate-Temperature MS–SOFCs

2.1 Introduction

Metal-supported solid oxide fuel cells (MS–SOFCs) offer many advantages like excellent structural robustness and stability, high tolerance toward rapid thermal cycling, easy stack assembling as well as low materials cost over the conventional all-ceramic structured solid oxide fuel cells (SOFCs) [1–3]. Such advantages benefit from the mechanically robust, electrically and thermal conductive metals applied in the metal-supported construction. However, employing metals, e.g., stainless steel as the support may bring a number of challenges to the cell fabrication processes, especially the densification of electrolytes and the fabrication of electrodes.

Densification of electrolyte materials like yttria stabilized zirconia (YSZ) requires high temperatures (usually above 1200 °C). However, serious oxidation of the metal substrate will happen at the high sintering temperatures. Co-firing the metal support and electrolyte in a reducing atmosphere can solve the problem, while electrolytes like doped ceria and strontium and magnesium doped lanthanum gallate (LSGM) are not stable under the reducing atmosphere at high temperatures. Meanwhile, elements inter-diffusion between the ferritic FeCr substrate and nickel-containing anode, e.g., iron and chromium from the ferritic substrate into the anode and nickel from the anode into the ferrite is a serious problem resulting in the low power density and rapid performance degradation of MS–SOFCs [4, 5]. Furthermore, fabrication of the cathode layer is also challenging for MS–SOFCs since the commonly used cathode materials such as $La_{1-x}Sr_xMnO_{3-\delta}$ (LSM) and $La_{1-x}Sr_xCo_{1-y}Fe_yO_{3-\delta}$ (LSCF) would decompose when sintered at high temperatures in a reducing atmosphere that is required to protect the stainless steel substrates from excessive oxidation. Such processing challenges make the electrochemical performance and stability of the most MS–SOFCs much lower than those of the traditional all-ceramic structured SOFCs. Even though techniques like plasma spray and pulsed laser deposition (PLD) are applied to the MS–SOFCs

© Springer Nature Singapore Pte Ltd. 2018

Y. Zhou, *Study on Fabrication and Performance of Metal-Supported Solid Oxide Fuel Cells*, Springer Theses, https://doi.org/10.1007/978-981-10-6617-7_2

preparation processes, such methods would either increase the fabrication costs or sacrifice the cell performances [6–11].

Due to the above issues, most state of the art MS–SOFCs operate at temperatures around 800 °C, these high temperatures may cause problems like substrate oxidation and performance degradation. How to reduce the operation temperature of MS–SOFCs with YSZ electrolyte to intermediate-temperatures (600–800 °C) via a simple and low-cost method is a real problem. In recent years, the infiltration method has been applied into the manufacture of MS–SOFCs [1, 12–14]. This method involves preparing a porous backbone, e.g., yttria-stabilized-zirconia (YSZ) backbone which has been sintered at a high temperature (around 1300 °C). The second component of the electrode is then introduced into the porous backbone by infiltrating and subsequent oxidizing or reducing at a low temperature (350–850 °C). The infiltration method not only avoids the high-temperature process but also enables promising cell performances for the resulting nano-structured catalysts.

Here we design a novel MS–SOFC based upon tri-layers-porous 430L substrate | dense YSZ electrolyte | porous YSZ backbone-with Ni/$Ce_{0.8}Sm_{0.2}O_{2-\delta}$ (SDC)/Ni–SDC catalysts infiltrated into the porous 430L substrate as the anode and $La_{0.6}Sr_{0.4}Fe_{0.9}Sc_{0.1}O_{3-\delta}$ (LSFSc) catalysts infiltrated into the porous YSZ backbone as the cathode, respectively. This simplified tri-layer-structure not only reduces the cell manufacturing processes but also eliminates the resistances caused by additional barrier layers. Moreover, since the active electrode catalysts are deposited into the pre-sintered backbones at relatively low temperatures, problems like elemental inter-diffusion and stainless steel oxidation could be avoided.

2.2 Experimental Section

2.2.1 Technical Route

The schematic of the technical route for the manufacturing of MS–SOFCs is shown in Fig. 2.1. Firstly, green tapes based upon tri-layers-metal support (pore formers containing) | YSZ electrolyte | YSZ electrolyte (pore formers containing) were fabricated by the tape casting and laminating techniques. Secondly, the green tapes were co-sintered at a high temperature (around 1300 °C) under the reducing atmosphere and a structure of "porous metal support | dense YSZ electrolyte | porous YSZ" was obtained. Thirdly, precursor solutions of the anode and cathode materials were infiltrated into the porous metal support and the porous YSZ layer, respectively. Lastly, a low-temperature heat treatment (350–850 °C) was conducted to convert the precursors into nano particles acting as active electrode materials for the MS–SOFCs.

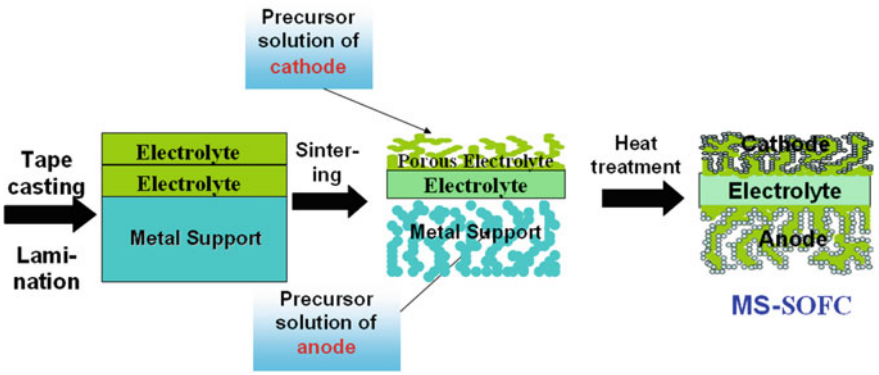


Fig. 2.1 Schematic of the production process for the manufacturing of MS–SOFCs

2.2.2 *Fabrication of Symmetric and Single Cells*

For single cell preparation, commercial 430L stainless steel powder (−400 mesh, Jing-yuan Powder Material Co., Ltd, China) and 8YSZ powder (Tosoh Corporation, Japan) were used as starting materials. The slurry for tape casting was ethanol based which contained pore-forming agent, dispersing agent, binder, plasticizer and other organic additives, in addition to powders. The simple tri-layer structure of porous 430L | YSZ electrolyte | porous YSZ backbone was produced by laminating tape cast green tapes and subsequent co-firing at 1300 °C for 4 h in a reducing atmosphere (5% H_2/95% N_2). Symmetric anode and cathode cells were prepared similarly, based upon "porous 430L | YSZ electrolyte | porous 430L" and "porous YSZ | YSZ electrolyte | porous YSZ", respectively. Both the symmetric anode and cathode cells were supported by a dense YSZ electrolyte with the thickness of 200 μm. For the symmetric anode cell, the thickness of the porous 430L was 80 μm. While for the symmetric cathode cell, the thickness of the porous YSZ was 40 μm.

For cathode catalysts, LSFSc particles were introduced into the porous YSZ backbones by infiltrating aqueous solutions containing stoichiometric amounts of La$(NO_3)_3$, Sr$(NO_3)_2$, Fe$(NO_3)_3$ and Sc$(NO_3)_3$, where citric acid was also added at a 1:1 molar ratio to metal ions. After drying, heat treatment was conducted at 850 °C in a reducing atmosphere of 5% H_2–95% N_2 for 2 h to convert these salts into metal oxides without excessive oxidation of the 430L substrate. While for the anode, Ni$(NO_3)_2$, Sm$(NO_3)_3$ and Ce$(NO_3)_3$ aqueous solution in stoichiometric ratios (the mass ration of SDC:Ni = 8:2/1:0/0:1) was also introduced into the porous 430L support by the infiltration method after the cathode preparation. Heat treatment of the anode catalysts was conducted at 600 °C. The loadings of infiltrated catalysts were controlled by a micro-liter syringe each time and the infiltration/heat treating cycle was

repeated to achieve the ultimate loadings needed. A single infiltration/heat treating cycle yielded the loading of ≈5 wt% for cathode and ≈3 wt% for anode.

2.2.3 Material Characterizations

The phases of infiltrated electrodes were identified by a Rigaku XRD diffractometer at room temperature, using monochromatic CuKα radiation. The microstructures of cells were studied using scanning electron microscopy (SEM) in S-4800-II microscopes. The porosities and pore-size distributions of porous 430L substrates and YSZ backbones were measured using mercury intrusion porosimetry carried out with a Micromeritics Auto Pore IV 9500 V1.09. Atomic diffusions were analyzed using a JEOL JXA-8100 electron probe microanalyzer (EPMA). In situ X-ray diffraction was performed on a Bruker–D8 advanced X-ray diffractometer equipped with an Anton Paar HTK1200 using Cu K_α radiation source. During the experiments, the as-synthesized powders were annealed in air and 5% H_2–95% Ar at an interval of 50 °C between 600 and 750 °C. The diffraction patterns were collected with a step of 0.02^o over the range of 20–80^o. The reduction behavior of as-synthesized SDC powders was studied by hydrogen temperature-programmed reduction (H_2–TPR) using Micromeritics ChemiSorb 2720 instrument. Specifically, 20 mg of powders were packed in a U-type quartz reactor and degassed in He at 350 °C for 0.5 h, followed by cooling to 25 °C under He flow. The H_2–TPR profile was collected in a stream of 5% H_2–95% Ar (30 sccm) at a ramp rate of 5 °C/min up to 1000 °C. The effluent gas was analyzed by a thermal conductivity detector (TCD).

2.2.4 Electrochemical Measurements

For electrochemical measurements, single fuel cells were sealed onto alumina tubes using silver paste (DAD–87, Shanghai Research Institute of Synthetic Resin). Silver grids were applied onto electrodes as current collectors with silver wires attached as the voltage and current leads. Current–voltage curves were obtained using an IM6 Electrochemical Workstation (ZAHNER, Germany) at 600–800 °C with cathodes exposed to air and anodes to humidified (3% H_2O) hydrogen both at 100 sccm. Electrochemical impedance spectra (EIS) were collected at open circuits with 20 mV AC amplitudes over the frequency range of 0.02 Hz–0.2 MHz. Impedance measurements were also performed in air on symmetric cathode cells or in humidified (3% H_2O) hydrogen on symmetric anode cells. Active areas of the single cell, symmetric anode cell and symmetric cathode cell were 0.35, 0.7 and 0.35 cm^2, respectively.

2.3 Results and Discussion

2.3.1 *Investigation of Infiltrated LSFSc–YSZ Cathodes*

Figure 2.2 shows the XRD patterns of the infiltrated LSFSc–YSZ cathode as obtained with subsequent oxidation at 800 °C for 2 h in air and formation of the LSFSc perovskite oxide is confirmed [15].

The polarization resistances of the infiltrated LSFSc–YSZ composite cathodes measured at 800 °C in air with the LSFSc loadings ranging from 20 to 40 wt% are shown in Fig. 2.3a. It can be found that the composite cathode with the LSFSc loading of 30 wt% exhibits the lowest polarization resistance of 0.024 Ω cm^2. Such result is lower than the LSCF or LSF infiltrated YSZ cathode as reported before [16, 17]. Note that both the polarization resistances of LSFSc loadings lower and higher than 30 wt% are much larger than that of the 30 wt% loading. It can be explained by the three-phase boundary (TPB) dependence of the infiltrated loadings. Model study indicates that the total and active TPB lengths initially increase with increasing infiltration loading, reach a maximum value, and then decrease with a further increase in infiltration loading due to the contact between the infiltrated nano particles [18]. EIS of infiltrated LSFSc–YSZ cathodes with different LSFSc loadings in Fig. 2.3b, c indicate the reducing of polarization resistance (mainly in the intermediate- and high-frequency range) when the LSFSc loading increases from 20 to 30 wt%. While further increasing the loading to 35 and 40 wt%, enlarged intermediate- and high-frequency arcs are shown. Since the intermediate-frequency arcs are frequently attributed to the oxygen surface reaction and high-frequency arcs to the charge transfer process [19], one possible explanation is that when the loading is lower than 30 wt%, infiltrated particles are not sufficient to build enough surface areas for surface oxygen adsorption and enough pathways for electron transfer, while when the loading is higher than 30 wt%, the aggregated LSFSc particles would reduce the effective TPB lengths of the LSFSc–YSZ composite electrodes. In contrast to the changeable intermediate- and high-frequency arcs, the small low frequency arcs attributed to the process of gas diffusion are relatively

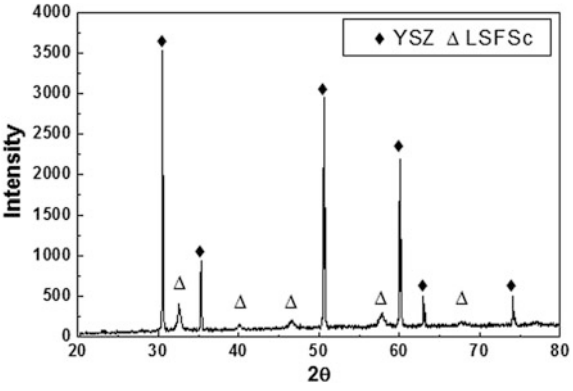


Fig. 2.2 XRD patterns of the LSFSc–YSZ cathode with subsequent oxidation at 800 °C in air. Reproduced with permission from Ref. [15]. Copyright 2014, The Electrochemical Society

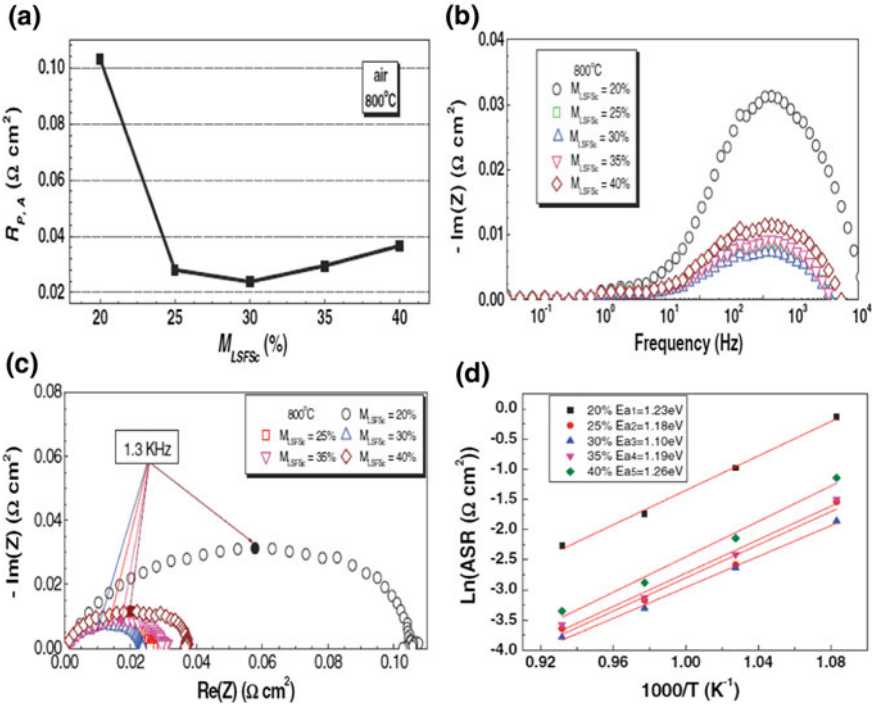


Fig. 2.3 **a** Polarization resistances, **b** Bode representations of EIS, **c** Nyquist representations of EIS and **d** Activation energies of the polarization resistances of the LSFSc–YSZ cathodes with different LSFSc loadings. Reproduced with permission from Ref. [15]. Copyright 2014, The Electrochemical Society

stable as observed in Fig. 2.3b, c. We surmise that the LSFSc loadings within the range of 20–40 wt% may not affect the gas diffusion process considering the high porosity of YSZ backbone (69%). Figure 2.3d shows the activation energies of the polarization resistances of the LSFSc–YSZ cathodes with different LSFSc loadings. As observed, the 30 wt% loading shows the lowest activation energy, e.g., 1.10 eV for 30 wt% while 1.18 eV for 25 wt% and 1.19 eV for 35 wt%.

In the cathode, oxygen is reduced to oxide ion via the following oxygen reduction reaction (ORR):

$$\frac{1}{2}O_2(g) + 2e^- = O^{2-} \tag{2.1}$$

In Kroger–Vink notation, it is:

$$\frac{1}{2}O_2(g) + 2e^- + V_{\ddot{O}} = O_O^{\times} \tag{2.2}$$

ORR is a complex multi-step reaction, including: the gas diffusion, adsorption and dissociation of oxygen on the surface of the cathode, and the charge transfer, etc. Specifically:

Diffusion and adsorption of the oxygen on the surface of the cathode:

$$O_2(g) \Leftrightarrow O_{2(ad)} \tag{2.3}$$

Dissociation of the adsorbed molecular oxygen into atomic oxygen:

$$O_{2(ad)} \Leftrightarrow 2O_{ad} \tag{2.4}$$

Charge transfer from the cathode to the atomic oxygen (reduction of the adsorbed atomic oxygen):

$$O_{ad} + \mathrm{e}^- \Leftrightarrow O_{ad}^- \tag{2.5}$$

Solid-phase migration of the oxide ion from the cathode to the TPB:

$$O_{ad}^- \Leftrightarrow O_{TPB}^- \tag{2.6}$$

Reduction of the monovalent oxide ion in the TPB:

$$O_{TPB}^- + \mathrm{e}^- \Leftrightarrow O_{TPB}^{2-} \tag{2.7}$$

Diffusion of the oxygen ion from TPB to the electrolyte, associated with a charge transfer process:

$$O_{TPB}^{2-} + V_{\ddot{O}} \Leftrightarrow O_O^{\times} \tag{2.8}$$

The widely used parameter to determine the rate-determining step of the ORR is the slope of the polarization resistance of the cathode as a function of oxygen partial pressure, following the relation:

$$R_P \propto P_{O2}^{-n} \tag{2.9}$$

When the value of n is 1, 1/2, 3/8, 1/4, 1/8 and 0, the corresponding rate-determining step of the ORR is (2.3), (2.4), (2.5), (2.6), (2.7) and (2.8), respectively [20–25]. Figure 2.4 shows the relations of polarization resistance to P_{O2}, and schematics of their corresponding ORR processes [26].

In order to gain insights into oxygen reduction kinetics and identify the rate-limiting step of the infiltrated LSFSc–YSZ cathode, impedance data were collected for the symmetric cathode cells with 30 wt% of LSFSc at varied temperatures and under varied oxygen partial pressures. These impedance data were further fitted with an equivalent circuit, Ro (R^H, CPE^H) (R^L, CPE^L), where Ro was the pure ohmic resistance due to the electrolyte and the electrodes, R^H and R^L were widths of the high- and low-frequency arcs, while CPE^H and CPE^L were the

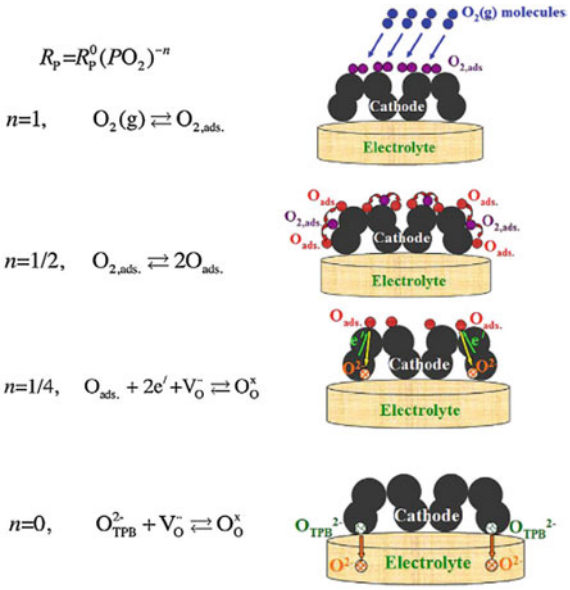


Fig. 2.4 The relations of polarization resistance to PO_2, and schematics of their corresponding ORR processes on the cathode. Reproduced with permission from Ref. [26]. Copyright 2014, Elsevier

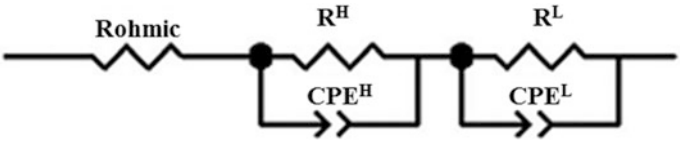


Fig. 2.5 Schematics of the equivalent circuit used for impedance spectra fitting

constant phase elements for the high- and low-frequency arcs, respectively (Fig. 2.5).

Figure 2.6 shows the Nyquist plots of the polarization resistances of the LSFSc–YSZ symmetric cells measured in air at different temperatures and oxygen partial pressures. The high-frequency value (R_{PC}^H) and low-frequency value (R_{PC}^L) as a function of temperature are shown in Fig. 2.7a. The R_{PC}^H value followed an Arrhenius dependence with an activation energy of 1.07 eV, while the R_{PC}^L value remained almost unaltered. It indicates that the high-frequency arc may associate with the charge transfer process in the interface of LSFSc and YSZ, and the low-frequency arc may relate to the diffusion and adsorption process of oxygen. This conclusion is further verified by the data measured under various oxygen partial pressures. As shown in Figs. 2.6b and 2.7b, a much more obvious oxygen partial pressure dependence of the low-frequency arcs was found than that of the

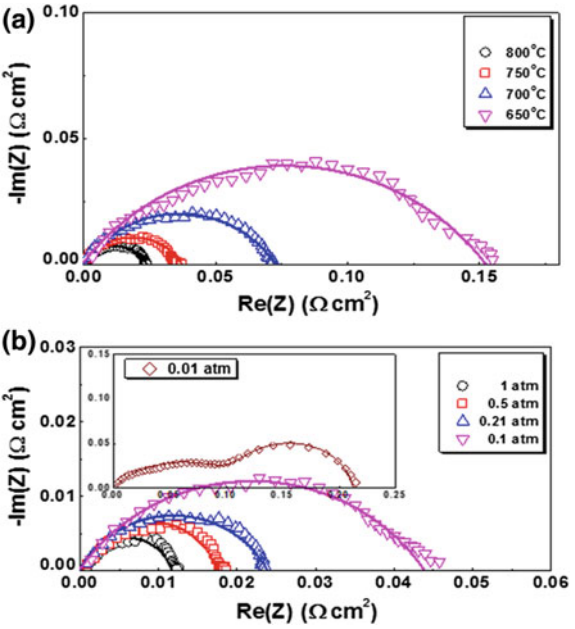


Fig. 2.6 Impedance plots of LSFSc–YSZ symmetric anode cells measured: **a** At 650–800 °C, **b** At 800 °C in atmospheres with different oxygen partial pressures

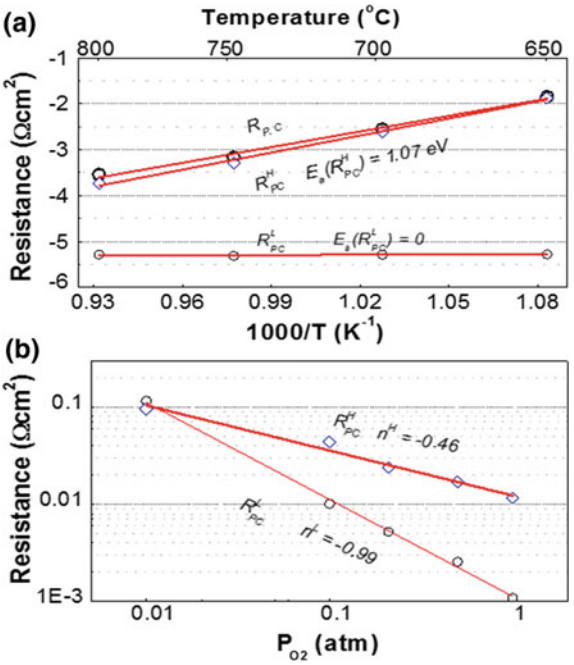


Fig. 2.7 **a** Temperature dependence of the R^H and R^L result, **b** Oxygen partial pressure dependence of the R^H and R^L result measured at 800 °C

high-frequency arcs. In addition, the R_{PC}^{H} value is much higher than the R_{PC}^{L} value in the oxygen partial pressure range of 0.21–0.1 atm, thus the ORR of the LSFSc–YSZ cathode is limited by the charge transfer process in the interface of LSFSc and YSZ.

2.3.2 *Investigation of Infiltrated Ni–430L Anodes and the MS–SOFCs*

Figure 2.8 shows the polarization resistances of the infiltrated Ni–430L anodes (calcining at 600 and 850 °C) measured at 650 °C in humidified hydrogen with the Ni loadings ranging from 4 to 16 wt% [27]. For the infiltrated Ni–430L anodes calcined at 600 °C, the Ni loading of 10 wt% exhibits the lowest polarization resistance of 2.2 Ω cm^2. Note that both the polarization resistances of Ni loadings lower and higher than 10 wt% are much larger than that of the 10 wt% loading. It can be explained by the three-phase boundary (TPB) dependence of the infiltrated loadings. Ni loadings dependence of the polarization resistances of the Ni–430L anodes calcined at 850 °C is also shown in Fig. 2.8. Different from the results of the anodes calcined at 600 °C, the optimized loading is 13 wt% for the anodes calcined at 850 °C. It can be explained that when the Ni particles are coarsened, connected particles tend to be isolated and an increased loading is needed to provide sufficient active surfaces for the hydrogen oxidation reaction [2].

Polarization resistances of the Ni–430L anodes obtained here are extraordinarily large compared to those of the Ni infiltrated doped $LaGaO_3$ anode, which only exhibited a low polarization resistance of 0.008 Ω cm^2 at 650 °C [28]. This is very likely caused by the short TPB length, which is only confined to the narrow YSZ–Ni contact area (marked in red in Fig. 2.9) closed to the YSZ electrolyte due to the absence of oxide-ion conducting components in the infiltrated Ni–430L anodes.

Impedance spectra of the infiltrated Ni–430L anode (10 wt% loading) calcined at 600 °C is shown in Fig. 2.10a. Notably, hydrogen oxidation kinetics is largely

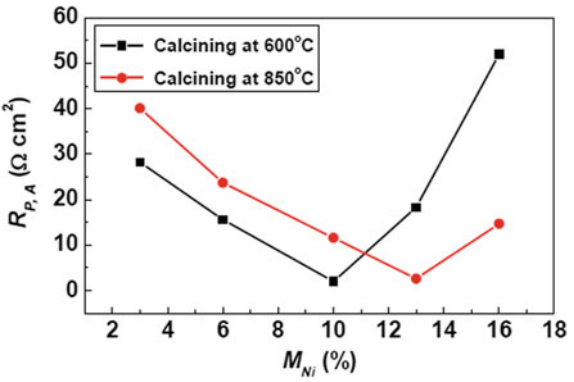


Fig. 2.8 Polarization resistances of the Ni–430L anodes with various Ni loadings tested at 650 °C. Reproduced with permission from Ref. [27]. Copyright 2014, Elsevier

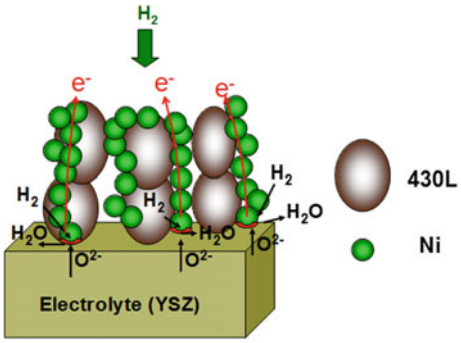


Fig. 2.9 Schematic diagram depicting the reaction pathways in Ni–430L anode

dominated by the charge transfer process with the summit relaxation frequency at 826 Hz, while the surface hydrogen exchange process is quick enough and makes little contributions to the anode polarization resistance since the arc commonly centered at 1 Hz is negligibly small. In order to evaluate the stability of the polarization resistance, the symmetrical anode cell was operated at 650 °C for about 50 h without current applied. The impedance spectra of the Ni–430L anode after the durability measurement is shown in Fig. 2.10b. Note that the anode polarization resistance increases drastically from 2 to 41 Ω cm^2 during the 50-h measurement and an increase in the lower-frequency is shown. Such increase is much more obvious in the Bode representations of the impedance data shown in Fig. 2.10c. It is reported that the higher-frequency arc is related to the charge transfer process near

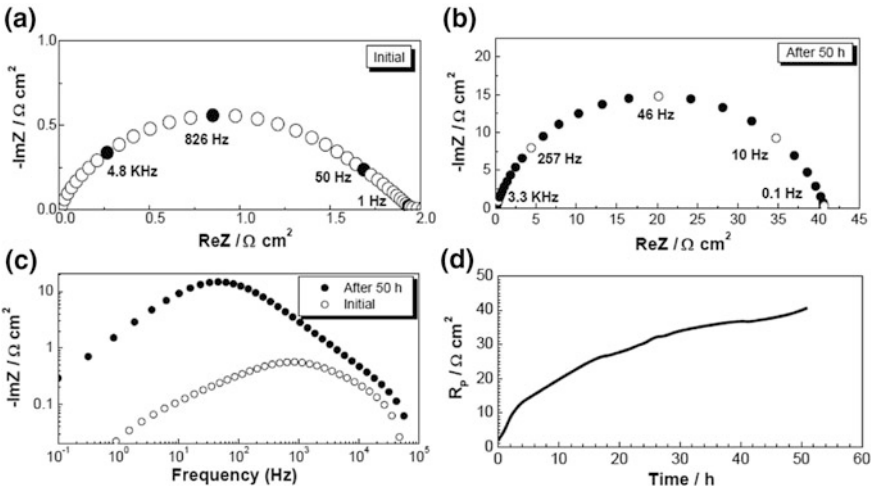


Fig. 2.10 Impedance data of the Ni–430L anodes calcined at 600 °C. Reproduced with permission from Ref. [27]. Copyright 2014, Elsevier

the TPB region, while the lower-frequency arc to the hydrogen dissociation adsorption or surface diffusion process on the Ni surface [14, 29, 30]. Since the infiltrated Ni particles are easy to be coarsened, the coarsening of Ni particles which decreasing the density of TPBs and active surfaces for hydrogen oxidation reactions may be the main reason to the increase of the anode polarization resistances [2, 19]. A sustained increase in the polarization resistance of the Ni–430L anode during the 50-h measurement is shown in Fig. 2.10d. For the large polarization resistance after the durability test, no extended measurement was applied.

Impedance spectra of the Ni–430L anode calcined at 850 °C (13 wt% loading) before and after the stability test are shown in Fig. 2.11a. A comparing of the impedance arcs in Figs. 2.10a and 2.11a (initial results) shows the similar arc shape and frequency distribution. It exhibits that coarsening of the Ni particles at 850 °C may not change the electrochemical process in the anode. However, the stability of

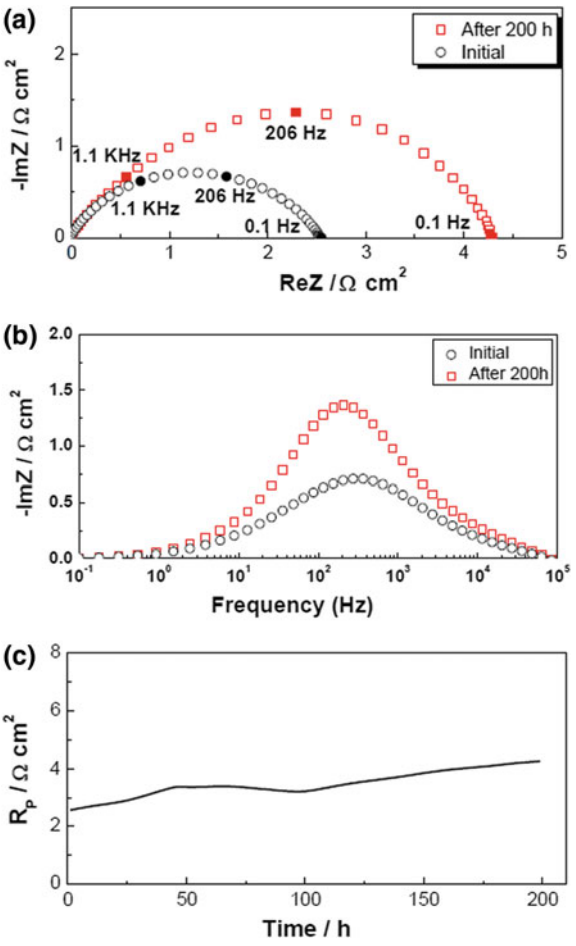


Fig. 2.11 Impedance of the Ni–430L anodes calcined at 850 °C. Reproduced with permission from Ref. [27]. Copyright 2014, Elsevier

the polarization resistance of the anode is improved and an increase from 2.6 to 4.3 Ω cm^2 during the 200-h measurement is exhibited in Fig. 2.11a. As shown in Fig. 2.11a, b, the increase of the polarization resistance mainly centered at the middle-frequency after the durability test. It indicates that the Ni particles may be further coarsened after the 200-h stability measurement. Compared to the rapid increase of the polarization resistance for the Ni–430L anode calcined at 600 °C, a much more slowly increase in the polarization resistance is shown for the anode calcined at 850 °C. This result illustrates that pre-coarsening of the infiltrated Ni particles can enhance the stability of the Ni–430L anode [2].

Scanning electron microscope (SEM) images of the Ni microstructures before and after the durability measurement are shown in Fig. 2.12. For the Ni calcined at 600 °C, pronounced particle growth is observed. In particular, well interconnected nickel layers (Fig. 2.12a) increase to the isolated coarsening particles after the stability test (Fig. 2.12b). Such phenomenon consists with the impedance spectra change shown in Fig. 2.10a, b. While for the Ni particles calcined at 850 °C, even the coarsening phenomenon is still observed (Fig. 2.12c, d), it is not so serious as that of the particles calcined at 600 °C. That may be the reason why the polarization resistance of the infiltrated anode calcined at 850 °C increases more slowly with time.

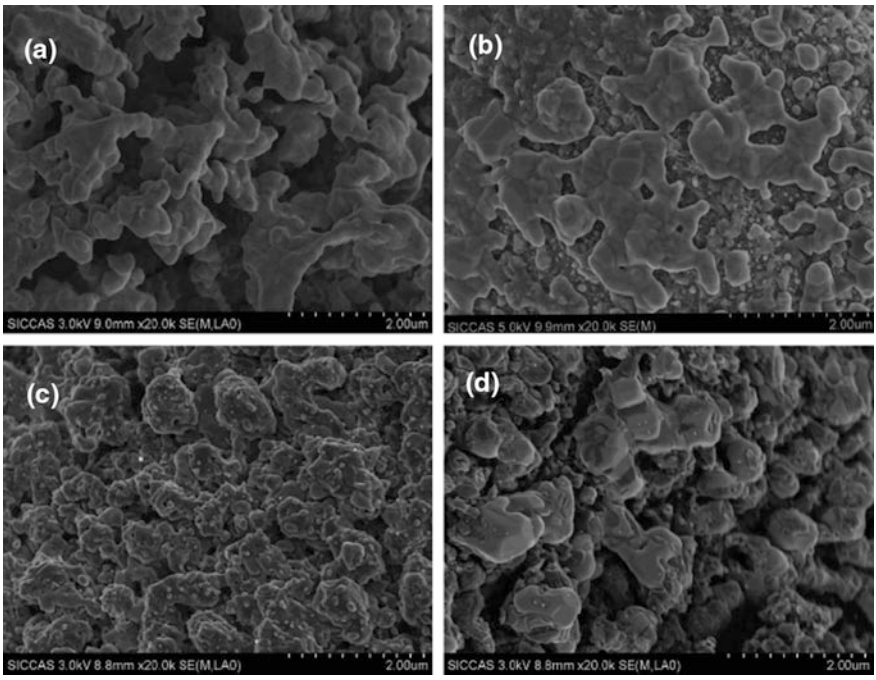


Fig. 2.12 Microstructures of the infiltrated Ni particles calcined at 600 °C: **a** Before and **b** after the stability test, microstructures of the infiltrated Ni particles calcined at 850 °C: **c** Before and **d** after the stability test. Reproduced with permission from Ref. [27]. Copyright 2014, Elsevier

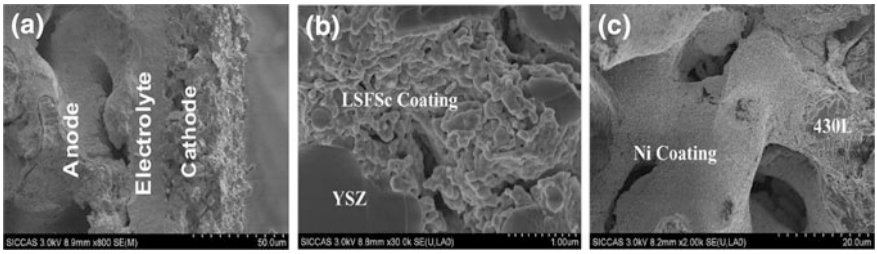


Fig. 2.13 SEM images of the: **a** MS–SOFC, **b** LSFSc–YSZ cathode, **c** Ni–430L anode. Reproduced with permission from Ref. [31]. Copyright 2014, Elsevier

MS–SOFCs based on the infiltrated Ni–430L anode and the LSFSc–YSZ cathode have been fabricated. Figure 2.13a shows a representative cross-sectional SEM micrograph of the single fuel cell with the infiltrated catalyst loadings of 10 wt % for the Ni anodes and of 30 wt% for the LSFSc cathodes. The YSZ electrolyte layer is fully dense with a typical thickness of ≈30 μm, and is well bonded with the adjacent 430L substrates and porous YSZ backbones. The porous YSZ backbone is 45 μm thick and the porous 430L substrate is 300 μm (part of the substrate is not shown in Fig. 2.13a). As shown in Fig. 2.13b, the infiltration of 30 wt% LSFSc is sufficient to produce well-interconnected coatings with an average particle size of 100 nm on the porous YSZ backbones. Porous 430L substrate with infiltrated Ni particles (10 wt% Ni loading) is also shown in Fig. 2.13c.

Figure 2.14a shows typical cell voltages and power densities as a function of current densities for the MS–SOFC operating on humidified hydrogen fuels and air oxidants at 650–800 °C. The open circuit voltage (OCV) is 1.06 V at 800 °C, indicating good gas impermeability of the dense YSZ electrolyte thin films as consistent with the SEM observations in Fig. 2.13a. The maximum power densities (MPDs) measured are 193, 418, 636 and 907 mW cm^{-2} at 650, 700, 750 and 800 °C,

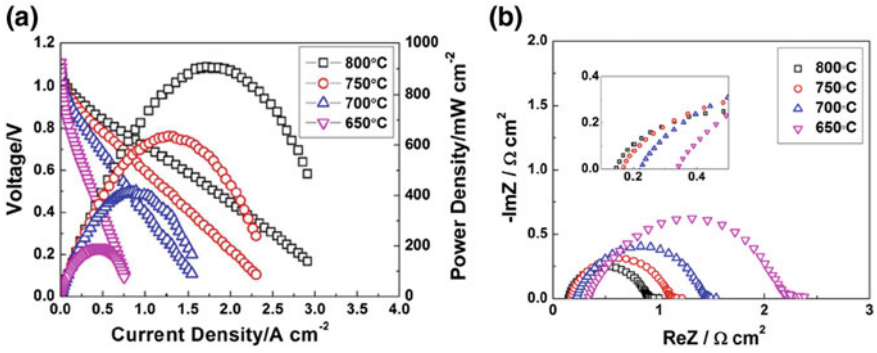


Fig. 2.14 Electrochemical characteristics of the single cell measured at 650–800 °C: **a** I–P–V characteristics, **b** Impedance spectra at open circuits. Reproduced with permission from Ref. [31]. Copyright 2014, Elsevier

respectively. These values are highly comparable with those previously achieved for alternative MS–SOFCs as fabricated using low-temperature deposition method like plasma spraying [32]. For example, FeCrMnTi supported vacuum plasma sprayed (VPS) Ni–YSZ anode and YSZ electrolyte fuel cells with suspension plasma sprayed (SPS) LSCF–CGO cathode showed a power density of 798 mW cm^{-2} at 0.7 V (800 °C) with H_2/O_2 atmosphere on anode/cathode side [33]. Figure 2.14b shows Nyquist plots of impedance data as obtained at open circuits for the present MS–SOFCs, where the pure ohmic losses (R_O) were taken from the high-frequency real-axis intercepts and the combined anode and cathode polarization resistances (R_P) corresponded to the overall width of the depressed arcs. In particular, the pure ohmic losses are R_O = 0.34, 0.22, 0.17 and 0.15 Ω cm^2 (shown in the magnified figure), and the total interfacial polarizations are R_P = 2.04, 1.32, 1.05 and 0.85 Ω cm^2 at 650, 700, 750 and 800 °C, respectively. Compared to the relatively small ohmic losses, the cell performances are largely limited by the polarization resistances.

In order to examine the long-term stability of the nano-scale catalysts, the present MS–SOFC was operated for 200 h under a constant terminal voltage of 0.7 V at 650 °C. Figure 2.15a shows a constant decrease of the current density from 190 to 147 mA cm^{-2}. Figure 2.15b compares Nyquist plots of the impedance data taken at open circuits before and after the durability test, indicating that the ohmic losses remain nearly unchanged while the total interfacial polarization resistances increase from 1.49 to 5.43 Ω cm^2. The degradation rate for the present fuel cells as estimated from Fig. 2.15a is ≈11%/100 h, which is much lower than that of prior MS–SOFCs with infiltrated Ni catalysts operated at a higher temperature of 700 °C with the power density dramatically decreasing from ≈250 to ≈50 mW cm^{-2} during a 15-h measurement [2]. Nevertheless, the present degradation rate is substantially larger than the value of 1%/1000 h as obtained at the same temperature for MS–SOFCs with co-infiltrated $Ce_{0.8}Gd_{0.2}O_{2-\delta}$-Ni anode catalysts during a 3000-h durability measurement [34].

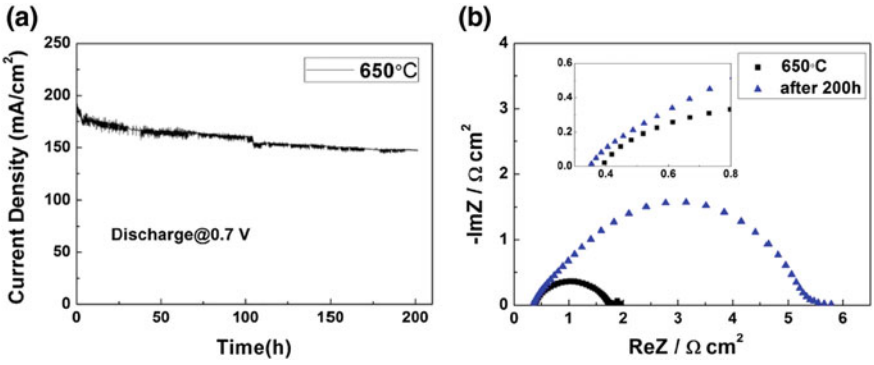


Fig. 2.15 **a** Stability of the single cell measured at 650 °C, **b** Impedance spectra of the single cell measured before and after the stability test. Reproduced with permission from Ref. [31]. Copyright 2014, Elsevier

As shown in Fig. 2.15b, it is the increased total interfacial polarization resistance that yields the large drop in the cell power density. To identify the individual contributions of the anode and the cathode to such an increase in the total polarization resistance, impedance measurements were also performed on the symmetric cathode and the symmetric anode cells over the long term, and the results are summarized in Fig. 2.16a, b, respectively. Notably, the anode polarization resistance increases drastically from 2 to 30 Ω cm^2 during the 30-h measurement at 650 °C. In contrast, the cathode polarization resistance stays almost unchanged over an even longer measurement of 400 h. Therefore, formation of insulating impurities and coarsening of nano-scale catalysts, which are normally identified as the two main reasons for decreased catalytic activities and increased polarization resistances of the infiltrated cathodes, did not occur for the present LSFSc–YSZ composites at 650 °C [35, 36]. Good stability in the nano-scale LSFSc catalysts is further supported by the SEM examination of the cathode microstructure before and after the durability measurement (Fig. 2.17a, b), where no pronounced increase in the particle size or change in the particle morphology is observed. On the other hand, pronounced growth in the nano-scale Ni catalysts is observed for the Ni–430L composites. In particular, well interconnected nickel particles with an average particle size of 0.1–0.3 μm evolve into isolated and coarsened ones with particle size of 0.5–1 μm after the stability test (Fig. 2.17c, d). The morphological evolution of the Ni particles decreases the density of TPBs for hydrogen oxidation reactions and thereby increases the anode polarization resistances as shown in Fig. 2.16b.

Prior reports have shown that the metallic inter-diffusion between metal substrates and Ni based anodes may occur during the fabrication and operation of fuel cells, decreasing the anode catalytic activities and thus increasing the polarization resistances of the anodes [37, 38]. For example, diffusion depth of Fe and Cr in the nickel anodes was as large as 200 μm when heat-treated at 1400 °C for 2 h in 4% H_2–96% Ar [39]. In order to identify whether inter-diffusions of Fe, Ni and Cr occurred at the operating temperature of MS–SOFCs, porous Ni coatings were

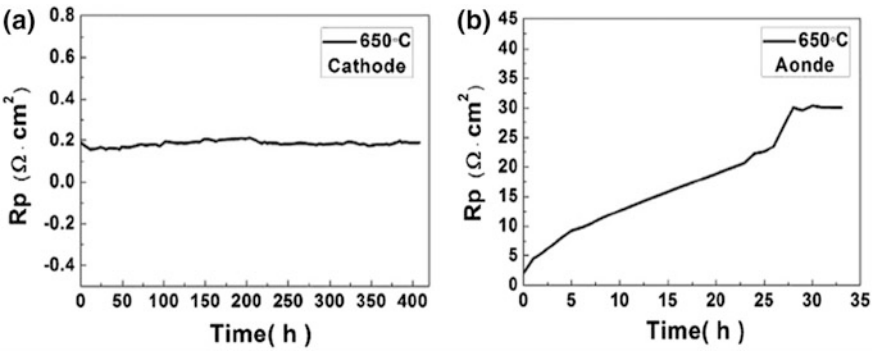


Fig. 2.16 Stabilities of the polarization resistances of the symmetric cells: **a** cathode, **b** anode. Reproduced with permission from Ref. [31]. Copyright 2014, Elsevier

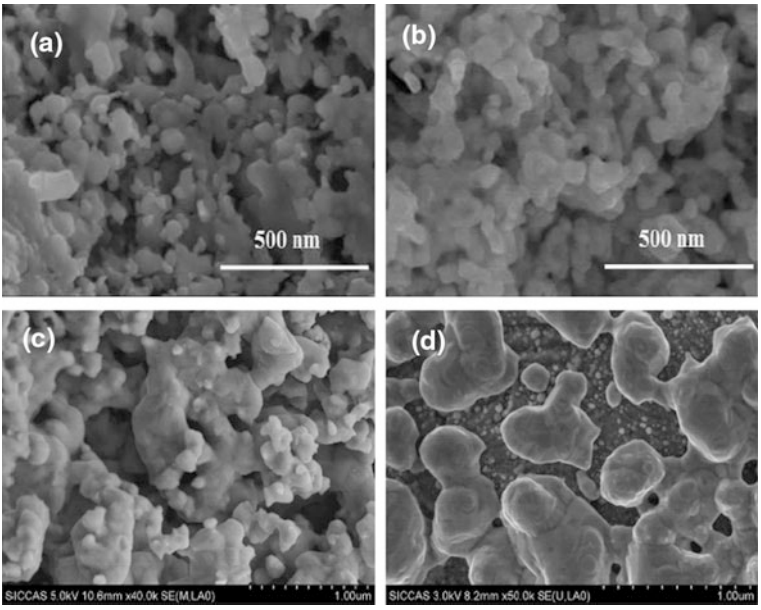


Fig. 2.17 Microstructures of the LSFSc particles: **a** Before and **b** after the stability test, microstructures of the Ni particles: **c** Before and **d** after the stability test. Reproduced with permission from Ref. [31]. Copyright 2014, Elsevier

electroplated onto the surface of commercial 430L plates and the resulting samples were thermally treated in 97% H_2–3% H_2O at 650 °C for 230 h. SEM examination shows that the Ni coating is well adhered onto the 430L substrate, and EDX analysis indicates that the Ni, Cr and Fe concentrations decrease gradually along the interfacial region of ≈30 μm thick between Ni and 430L (Fig. 2.18), which is

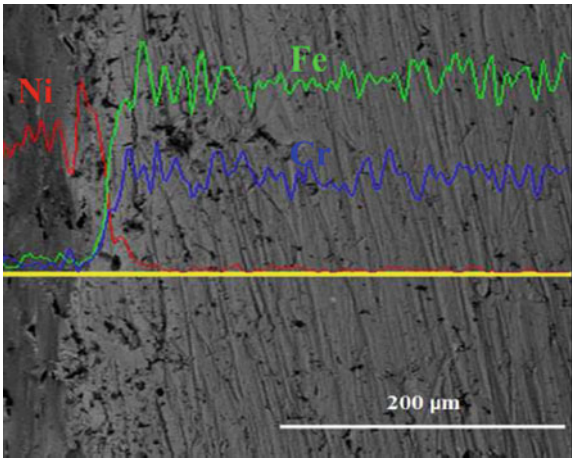


Fig. 2.18 Microstructure and elements distributions at the interface of Ni coating (*left*) and 430L background (*right*) after the heat-treatment at 650 °C for 230 h: Ni-*red*, Fe-*green*, Cr-*blue*. Reproduced with permission from Ref. [31]. Copyright 2014, Elsevier

probably caused by the inter-diffusions of Fe, Cr and Ni between the deposited Ni layer and the 430L substrate over the measurement period. Therefore, atomic diffusion could also be one of the possible physical mechanisms for the cell degradation in addition to the Ni coarsening.

Other than Ni coarsening and metallic inter-diffusion, oxidation of the porous 430L substrates in humidified hydrogen could also increase the anode area specific resistance due to the formation of oxide scales and the metal/oxide scale interfaces [40, 41], especially given that the present 430L substrates have increased surface area available for oxidation than the dense counterpart [42]. Note that the ohmic losses remained constant during the long-term measurements for the functioning single cells (Fig. 2.15b), indicating that the resulting scales had sufficiently high conductivities or the oxidation itself was not so serious at all. Furthermore, there is no obvious spalling observed between the Ni coatings and the 430L substrates as shown in Fig. 2.17d. Therefore, based upon the present preliminary durability measurement, oxidation of the 430L substrates might not be a significant issue for the present fuel cells. This conclusion is consistent with previous reports that 430L can achieve the oxidation rates required for the fuel cell lifetime of 50,000 h when the operating temperature is within the range of 650–700 °C [1].

2.3.3 *Investigation of Infiltrated SDC–430L Anodes and the MS–SOFCs*

The infiltrated Ni–430L anode showed a good electrochemical performance when applied in MS–SOFCs. However, the application of such anodes is hindered by the performance degradation caused by the Ni coarsening and metallic inter-diffusion issues. Thus, a ceramic anode with a good morphological and chemical stability should be taken into consideration. Ceria and ceria-based oxides are attractive as the SOFC anode catalysts due to their excellent redox and catalytic properties, as enabled by the distinctive feature of cerium ions to easily switch between Ce^{4+} and Ce^{3+} in different atmospheres [43–46]. In this section, $Ce_{0.8}Sm_{0.2}O_{2-\delta}$ (SDC) is applied as the infiltrated anode catalysts and the particle coarsening and metallic inter-diffusion issues can be avoided, thus, the high long-term stability is expected.

The SDC powder was synthesized by calcining the infiltration solution in air at 800 °C for 2 h. Cubic particles with a particle size of 40–140 nm are shown in Fig. 2.19.

The interaction of SDC nano-particles with H_2 was examined by performing temperature-programmed reduction (TPR) in a 5% H_2–Ar gas flow, with a typical TPR profile shown in Fig. 2.20a. Two hydrogen consumption peaks, one at 633 °C and the other at 932 °C are observed due to different oxygen binding energies in the fluorite lattice. The peak at low temperatures is usually attributed to the formation of surface hydroxyl and removal of surface oxygen (i.e., reduction of surface cerium ions), whereas the peak at high temperatures is normally due to bulk

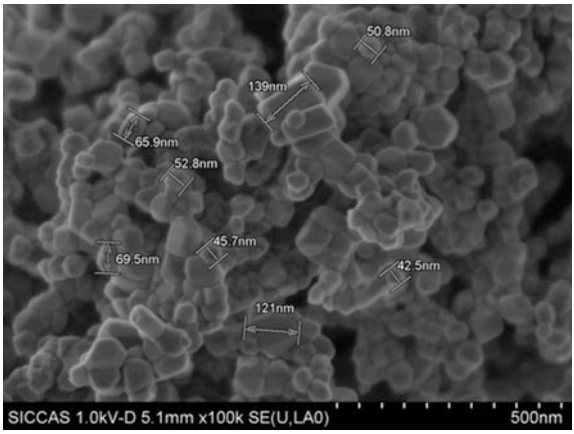


Fig. 2.19 Microstructure of the SDC powder as synthesized

reduction of Ce^{4+} to Ce^{3+} [47]. Nearly the same intensity for these two peaks suggests that nano-scale SDC catalysts have significant amounts of surface oxygen to be extracted by hydrogen. This fact can be well understood by large area-to-volume ratios of nano-scale SDC particles and high mobility of oxygen anions in the SDC lattice that would make bulk oxygen more readily available for surface extraction via diffusive jumps of free oxygen vacancies. The total amount of the releasable surface oxygen is 0.315 μmol per gram of SDC as estimated from the TRP profile in Fig. 2.20a.

The reduction behavior of SDC nano-particles in Fig. 2.20a was also reflected in the evolution of their crystal structure. In situ high temperature X-ray diffraction (XRD) measurements indicate that the cubic fluorite crystal structure was well maintained in H_2 (Fig. 2.21). Temperature-dependent evolution of the reflection peak (111) is shown in Fig. 2.20b, c for SDC oxides in hydrogen and air, respectively. Figure 2.20d summarizes the lattice parameter at different temperatures, as calculated from the Bragg angle of (111) peak in Fig. 2.20b, c. In contrast to a linear increase of the lattice parameter in air with increasing temperature, an abrupt expansion is observed in hydrogen at temperatures above 600 °C. This phenomenon should be related to irreversible association of adjacent surface hydroxyl to release gaseous water molecules that results in a reduction of cerium ions from Ce^{4+} to Ce^{3+} and a concomitant chemical expansion of the lattice due to larger radius for Ce^{3+} (0.114 nm) than for Ce^{4+} (0.097 nm) [48]. Such a lattice expansion behavior well coincides with the low-temperature hydrogen consumption peak with T_m = 633 °C in the TPR profile shown in Fig. 2.20a.

The sintered 430L scaffolds, as examined using the SEM, show a macroporous structure with the pore size distribution ranged widely from 4 to 90 μm (Fig. 2.22a, b). Mercury porosimetry measurements show an open porosity of 44% with pore sizes largely centered at ≈17 μm. Then, the porous 430L scaffolds were immersed into aqueous solutions containing $Sm(NO_3)_3$, $Ce(NO_3)_3$ and citric acid to produce thin SDC coatings after calcining in hydrogen at 800 °C. Figure 2.22c shows a

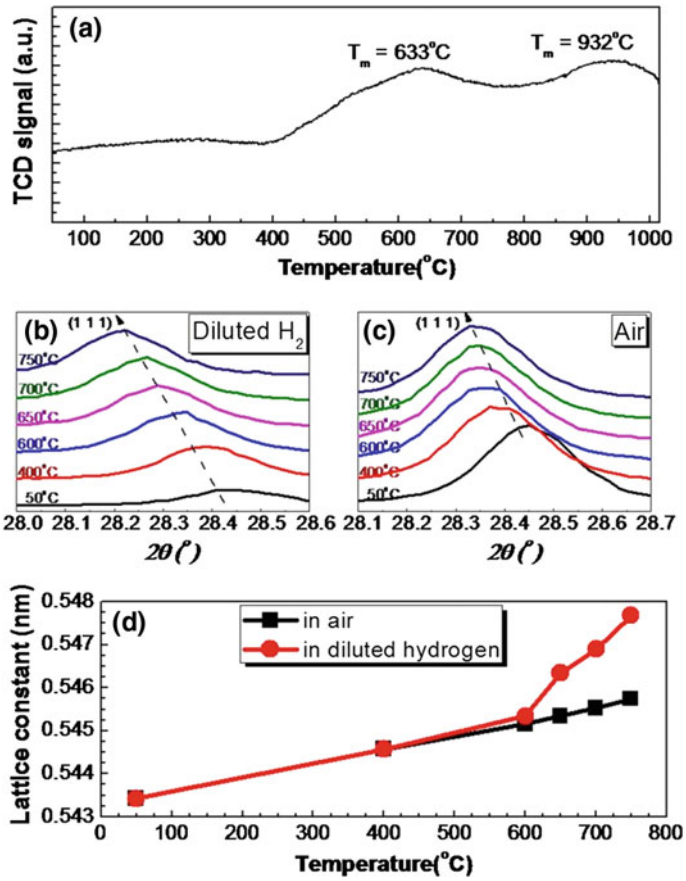


Fig. 2.20 Reduction behavior of the SDC catalysts: **a** TPR profile, Evolution of the (111) peak at elevated temperatures for XRD patterns in **b** 5% H_2–95% Ar and **c** air, **d** Temperature evolution of the lattice parameter as calculated (111) peaks shown in **b** and **c**

typical cross-sectional SEM image of the resultant composites, indicating that nanoporous SDC layers are homogeneously coated inside the macropores of 430L scaffolds. Close examination of the deposited SDC coatings (Fig. 2.22d) reveals a typical "cauliflower" structure, where the spherical agglomerates sizing from 60 to 110 nm appeared to consist of even finer particles of 10–20 nm in diameter. Upon increasing the calcining temperature to 1200 °C, these nanoscale particles grew dramatically and spread out on the 430L scaffolds to form dense thin films. SEM images for dense SDC–430L composites (Fig. 2.22e, f) show that such dense thin films consist of grains of 0.25–0.5 μm. Nonetheless, large surface-to-volume ratios of nanoporous SDC–430L composites would enable facile extraction of surface oxygen or reduction of surface cerium ions.

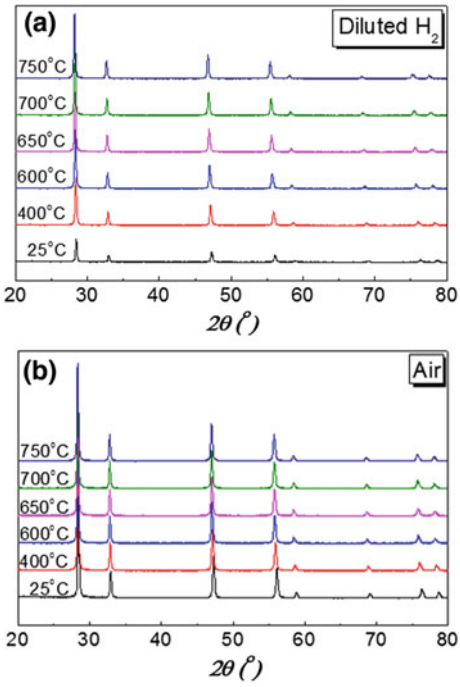


Fig. 2.21 XRD patterns of the SDC powder in: **a** Diluted H_2, **b** Air

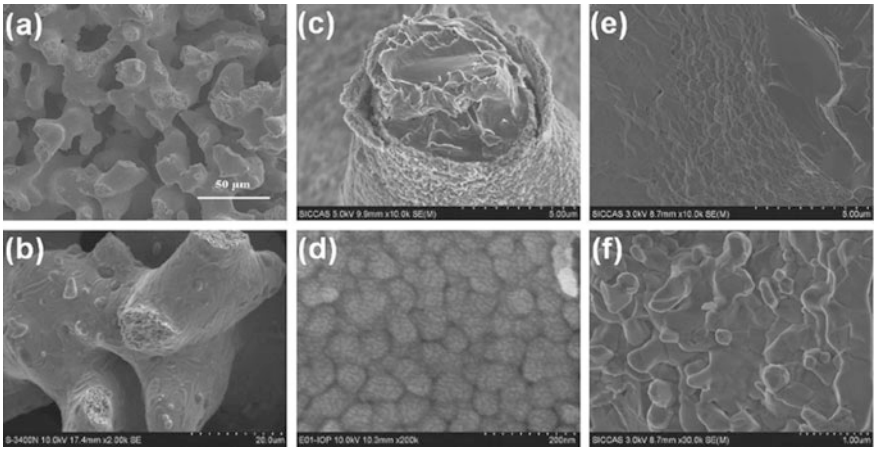


Fig. 2.22 Cross-sectional SEM images showing: **a** and **b** Blank 430L scaffold, **c** Nanoporous SDC–430L composites, **d** Nanoporous SDC catalysts, **e** Dense SDC–430L composite, **f** Dense SDC coatings. Reproduced with permission from Ref. [49]. Copyright 2014, Wiley-VCH

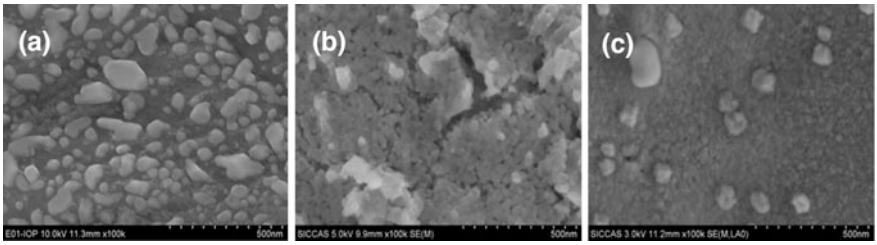


Fig. 2.23 SEM images of the surfaces of 430L with different SDC loadings: **a** 4 wt%, **b** 10 wt%, **c** 12 wt%

To optimize the performance of the SDC–430L anode, the relationship between the SDC loadings and the morphology, pore structure and polarization resistance of the anode was investigated. Figure 2.23 shows the morphology of the infiltrated SDC particles on the surface of the 430L backbone. At a loading of 4 wt%, only isolated SDC particles with size between 20 and 150 nm are shown (Fig. 2.23a). The isolated SDC particles further convert into nanoporous films when the loading increased to 10 wt% (Fig. 2.23b). However, further increasing the loading to 12 wt% resulted in dense SDC films with aggregated particles (Fig. 2.23c).

Figure 2.24 shows the pore size distributions of the 430L substrate before and after infiltrating of the SDC catalysts. It shows that porosities of the 430L substrate

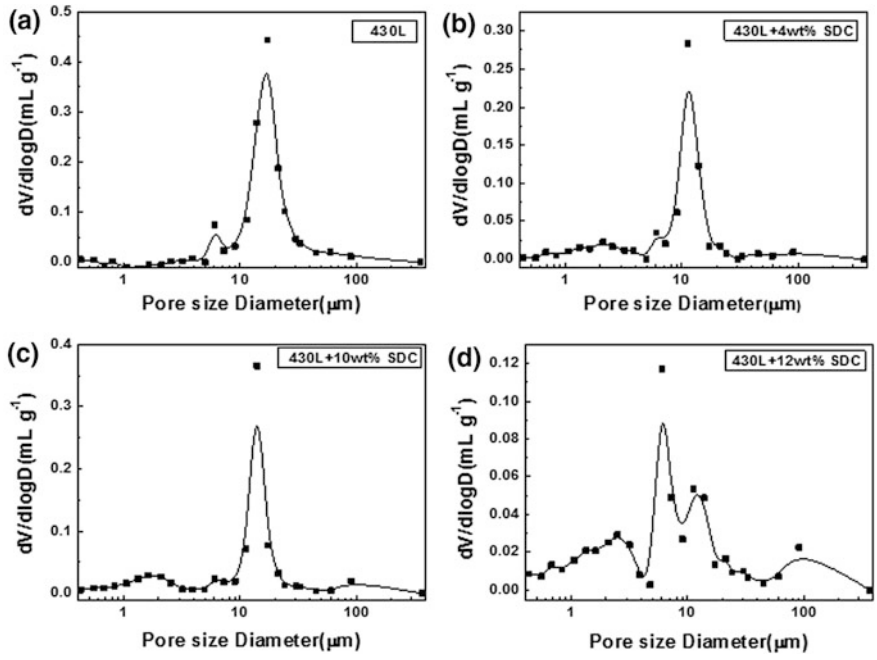


Fig. 2.24 Pore size distributions of the 430L substrate: **a** Blank 430L, **b** With a SDC loading of 4 wt%, **c** With a SDC loading of 10 wt%, **d** With a SDC loading of 12 wt%

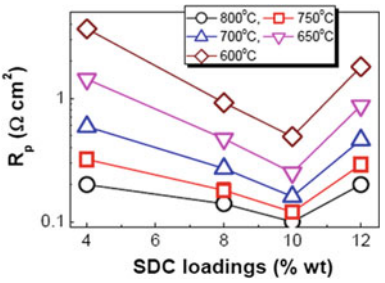


Fig. 2.25 Effect of SDC loadings on the polarization resistances of the SDC–430L symmetric anode cells

are 44.0, 34.5, 29.7 and 28.7%, and the main pore sizes are 17, 11, 14 and 6(11) μm when the loading of SDC are 0, 4, 10 and 12 wt%, respectively. A reduction in both the porosity and the pore size are shown as the loading of the SDC catalysts increased.

Figure 2.25 shows the polarization resistances of the infiltrated SDC–430L anodes with SDC loadings ranging from 4 to 12 wt%. Infiltrated SDC–430L anodes with a SDC loading of 10 wt% exhibits the lowest polarization resistance at all temperatures between 600–800 °C, which is reasonable given that reducing the catalyst loading would result in less active sites available for the hydrogen oxidation reaction, whereas increasing the catalyst loading would decrease the overall porosities and the TPB length in the anode (Figs. 2.23 and 2.24).

EIS of the polarization resistances of the infiltrated SDC–430L anodes with various SDC loadings are shown in Fig. 2.26. It is found that the difference of the EIS are mainly centered at a low-frequency range around 1 Hz. Since the low-frequency arc is mainly related with the surface process, it can be concluded that both the SDC loadings higher and lower than 10 wt% is not beneficial for the adsorption and dissociation of hydrogen on the surface of the SDC–430L anode.

As shown in Fig. 2.25, the polarization resistances of the infiltrated SDC–430L anodes (10 wt% loading) are 0.10 ± 0.01, 0.12 ± 0.02, 0.18 ± 0.03, 0.29 ± 0.06 and 0.57 ± 0.11 Ω cm^2 at 800, 750, 700, 650 and 600 °C, respectively. These values are competitive when compared with the polarization resistances reported for the common SOFC anodes, e.g., >0.15 Ω cm^2 at 750 °C for the traditional Ni–YSZ cermet anode [50], 0.26 Ω cm^2 at 900 °C for $La_{0.8}Sr_{0.2}Cr_{0.5}Mn_{0.5}O_{3-\delta}$ perovskite oxide [51], 0.27 Ω cm^2 at 800 °C for $Sr_2Fe_{1.5}Mo_{0.5}O_{6-\delta}$ double perovskite oxide [52], and 0.26 Ω cm^2 at 700 °C for the Pd-promoted $CeO_{2-\delta}$ infiltrated YSZ anode [53]. In contrast to the high resistance of the infiltrated Ni–430L anodes (2.2 Ω cm^2 at 650 °C, Fig. 2.8), an obvious decrease in the polarization resistance is shown. This should be caused by the enlarged TPBs from the narrow YSZ–Ni contact area to the whole surface of the infiltrated SDC particles (marked in red in Fig. 2.27) due to the good ionic and electronic conductivity of SDC under the reducing atmosphere.

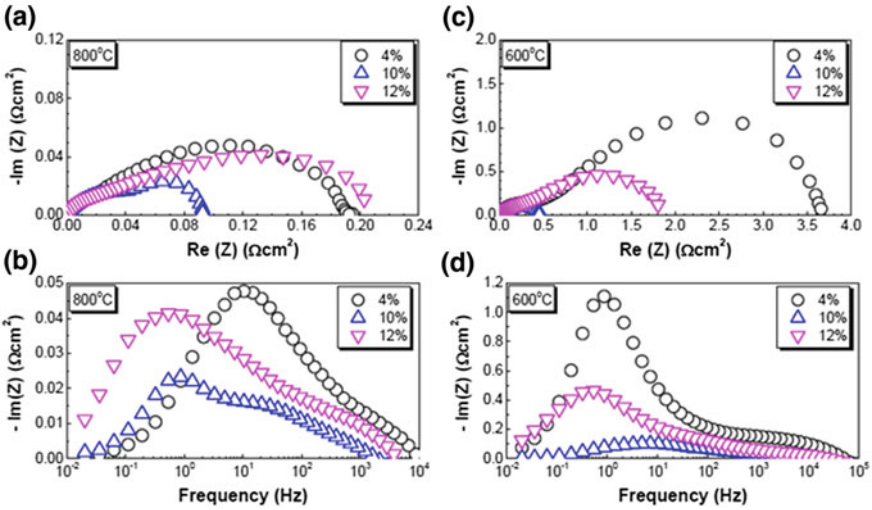


Fig. 2.26 EIS of the SDC–430L anodes with different SDC loadings: **a** Nyquist plots measured at 800 °C, **b** Bode plots measured at 800 °C, **c** Nyquist plots measured at 600 °C, **d** Bode plots measured at 600 °C

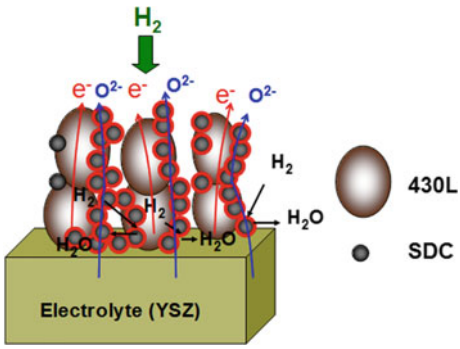


Fig. 2.27 Schematic diagram depicting the reaction pathways in SDC–430L anode

The overall anode reaction can be written in Kroger–Vink notation as follows:

$$H_2(g) + O_O^{\times}(YSZ) \rightarrow H_2O(g) + V_{\ddot{o}}^{\times}(YSZ) + 2e^{'}(430L) \tag{2.10}$$

Where $O_O^{\times}(YSZ)$ and $V_{\ddot{o}}^{\times}(YSZ)$ represent oxygen ions and oxygen vacancies in the YSZ lattice, respectively. Both quantum chemical molecular dynamic simulation and in situ surface studies revealed formation of surface hydroxyl ($OH_{\dot{O}}$) and reduction of Ce^{4+}($Ce_{Ce}^{'}$) for ceria in H_2 [54, 55], indicating that the global anode reaction on the infiltrated SDC–430L anodes might proceed in multiple consecutive or parallel steps as follows:

Dissociative adsorption of hydrogen molecules:

$$H_2(g) + 2O_O^{\times}(SDC) \rightarrow 2OH_O^{\times}(SDC) \tag{2.11}$$

Surface reduction of cerium ions:

$$OH_O^{\times}(SDC) + Ce_{Ce}^{\times}(SDC) \rightarrow OH_{\dot{O}}(SDC) + Ce_{Ce}^{'}(SDC) \tag{2.12}$$

Desorption of water molecules via association of adjacent surface hydroxyl:

$$2OH_{\dot{O}}(SDC) \rightarrow H_2O(g) + V_{\ddot{o}}(SDC) + O_O^{\times}(SDC) \tag{2.13}$$

Electron transport within SDC coatings and transfer to 430L:

$$Ce_{Ce}^{'}(SDC) \rightarrow Ce_{Ce}^{\times}(SDC) + e^{'}(430L) \tag{2.14}$$

Transport of oxygen vacancies within SDC coatings and transfer to YSZ electrolytes:

$$O_O^{\times}(YSZ) + V_{\ddot{o}}(SDC) \rightarrow O_O^{\times}(SDC) + V_{\ddot{o}}(YSZ) \tag{2.15}$$

Among these elementary steps, Reaction (2.14) and (2.15) are related to charge transport properties of the infiltrated SDC coatings since they transfer electrons and oxygen vacancies to 430L scaffolds and YSZ electrolytes, respectively. In contrast, Reaction (2.11), (2.12) and (2.13) are surface-related with the net result of removing surface lattice oxygen and reducing surface cerium ions from Ce^{4+} to Ce^{3+}. Figure 2.28a and b shows the Nyquist plots of the EIS data of the infiltrated SDC–430L anodes (SDC loading = 10 wt%) calcinated at 800 and 1200 °C, respectively. The two plots consist of two depressed arcs centered at ≈100 and ≈1 Hz, respectively. Evolution of infiltrated SDC coatings from nanoporous to dense yields a 5-fold increase in the high-frequency arc (R_H) and a 22-fold increase in the low-frequency arc (R_L). This observation, in combination with much stronger dependence of R_L values on hydrogen partial pressures (Fig. 2.29), suggests that the more surface-sensitive R_L value probably reflect extraction of surface lattice oxygen by hydrogen-Reaction (2.11), (2.12) and (2.13), whereas the less surface-sensitive R_H value is largely dictated by charge transport behavior of oxide-ions and electrons within the SDC coatings-Reaction (2.14) and (2.15). As a matter of fact, the activation energies for R_H and R_L values are essentially unaffected by the morphology of SDC coatings within the experimental uncertainty, i.e., 0.78–0.82 eV for R_H and 0.48–0.54 for R_L (Fig. 2.30). Comparing the activation energy for R_H with those for oxide-ionic conduction (≈0.80 eV) and for electronic conduction (1.3–2.3 eV) in ceria-based oxides implies that the R_H value is likely determined by transport of oxide-ions within the SDC coatings-Reaction (2.15) [56]. Prior mechanistic studies of hydrogen electro-oxidation on dense and patterned undoped ceria anodes have shown that Reaction (2.11) and (2.12) are kinetically fast and stay

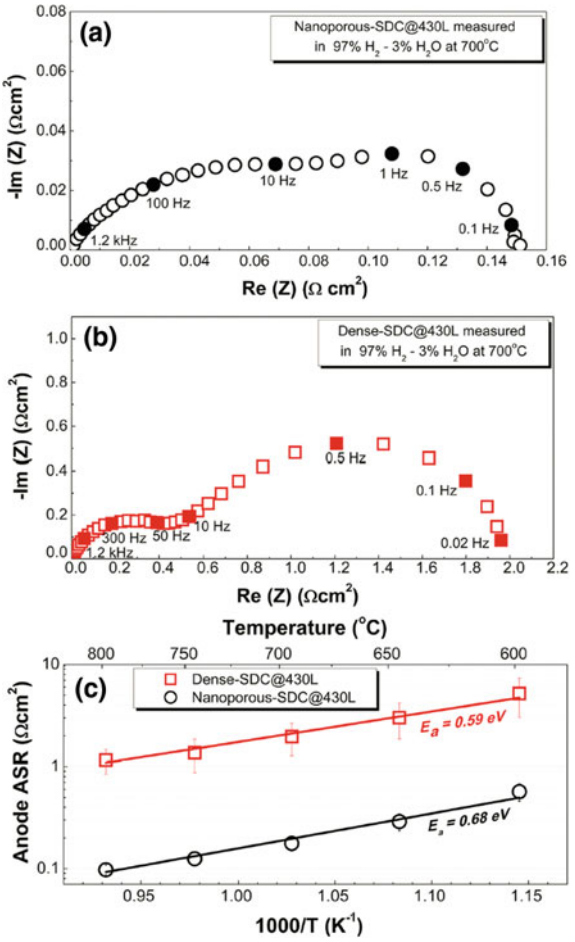


Fig. 2.28 Impedance spectra of the symmetric SDC–430L anode cells: **a** Nyquist plot for nano- porous SDC–430L anode, **b** Nyquist plot for dense SDC–430L anode, **c** Polarization resistance values for both anodes plotted versus inverse temperatures. Reproduced with permission from Ref. [49]. Copyright 2014, Wiley-VCH

in equilibrium while Reaction (2.13) is rate-limiting [55]. Therefore, the R_L value is more specifically dictated by desorption of water molecules via association of adjacent surface hydroxyl, Reaction (2.13). Several times larger R_L values than R_H for dense SDC infiltrated 430L anodes (Fig. 2.30) indicate that their hydrogen electro-oxidation kinetics is always dominated by surface desorption of water molecules. Nevertheless, the situation is quite different for nanoporous SDC infiltrated 430L anodes due to larger surface area to volume ratios, where hydrogen electro-oxidation is co-limited at high temperatures by surface desorption of water molecules and bulk transport of oxide-ions (Fig. 2.28a), with the latter becoming more important at lower temperatures due to larger activation energies (Fig. 2.30).

The anode catalytic activities of the infiltrated nanoporous SDC–430L anodes were further examined in the MS–SOFCs. Figure 2.31 shows the cross sectional SEM images of the MS–SOFC with SDC infiltrated in the 430L substrate (10 wt%)

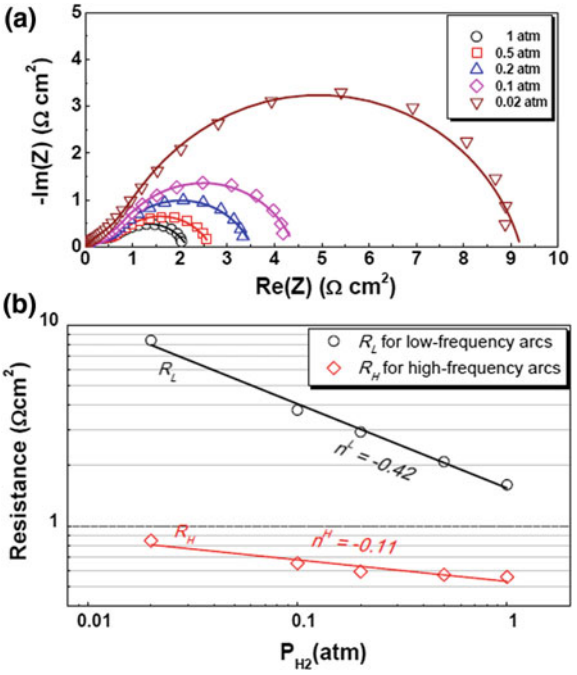


Fig. 2.29 **a** Nyquist plots of impedance data for the dense SDC–430L anode measured in various hydrogen partial pressures, **b** Hydrogen partial pressure dependence of the resistance values for the high- and low-frequency arcs. Reproduced with permission from Ref. [49]. Copyright 2014, Wiley-VCH

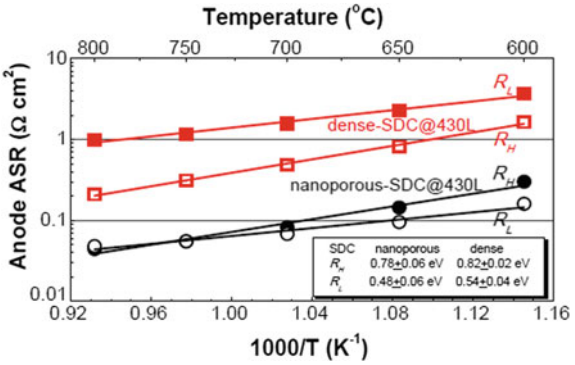


Fig. 2.30 The higher- and lower-frequency arcs of the impedance data for nanoporous SDC–430L and dense SDC–430L plotted versus inverse temperature. Reproduced with permission from Ref. [49]. Copyright 2014, Wiley-VCH

and LSFSc infiltrated in the YSZ backbone (30 wt%). Thickness for the dense YSZ electrolyte thin film is typically 25 μm. Nano porous SDC and LSFSc particles are found to be well attached with the porous backbones.

Electrochemical measurements were performed on the MS–SOFCs with 3% humidified hydrogen fuels and dry air oxidants at 650–800 °C, and Fig. 2.32a shows typical cell voltages and power densities as a function of current densities. The open circuit voltages range between 1.09 V at 650 °C and 1.04 V at 800 °C, and are within 50 mV of the thermodynamically expected Nernst potentials.

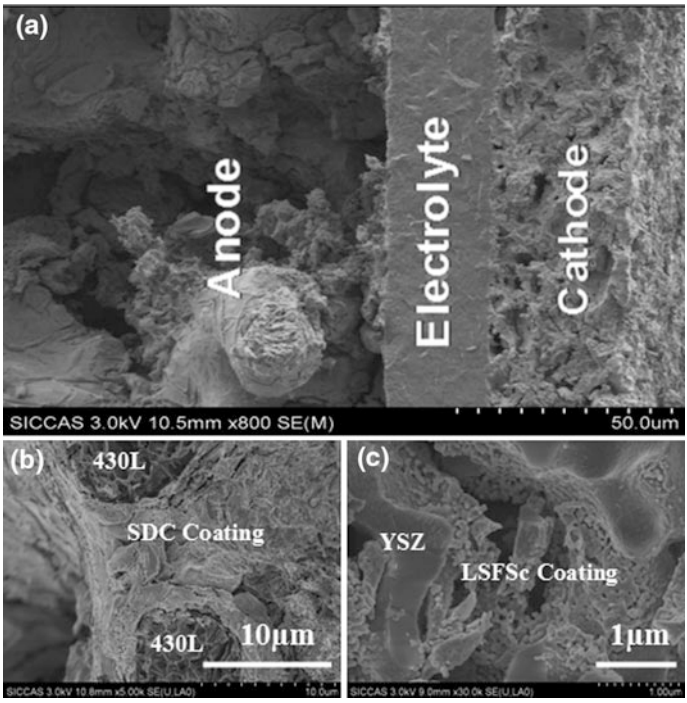


Fig. 2.31 SEM images of the: **a** MS–SOFC, **b** SDC–430L anode, **c** LSFSc–YSZ cathode

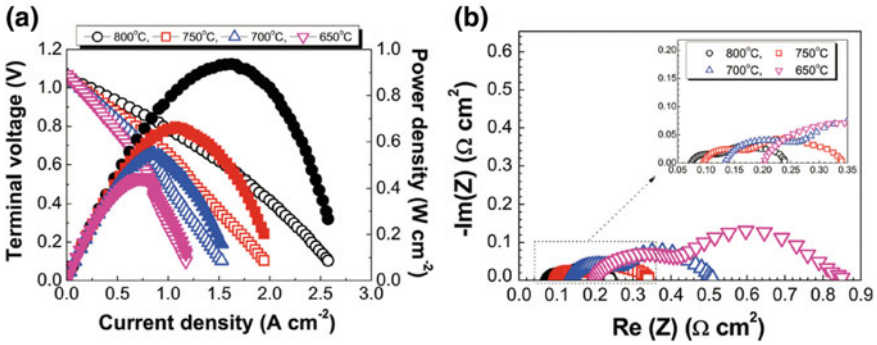


Fig. 2.32 Electrochemical characteristics of the single cell measured at 650–800 °C: **a** I–P–V characteristics, **b** Impedance spectra. Reproduced with permission from Ref. [49]. Copyright 2014, Wiley-VCH

Maximum power densities measured are 0.45, 0.55, 0.66 and 0.94 W cm^{-2} at 650, 700, 750 and 800 °C, respectively. Nyquist plots of the impedance data measured at open circuits (Fig. 2.32b) show that the total area specific resistances are 0.239, 0.340, 0.509 and 0.851 Ω cm^2 and the ohmic losses (R_O) are 0.073, 0.097, 0.133

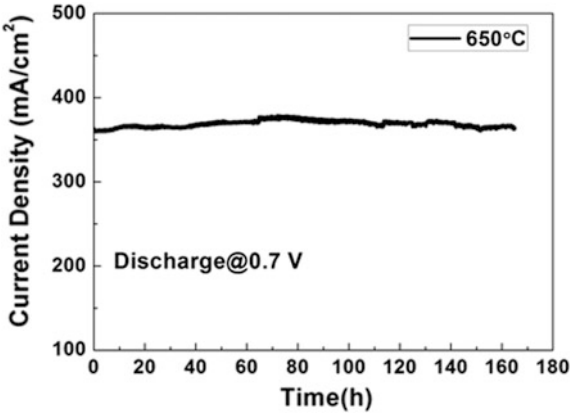


Fig. 2.33 Stability of the single cell measured at 650 °C

and 0.202 Ω cm^2 at 800, 750, 700 and 650 °C, respectively. It can be found that the resistances of the single cell mainly dominated by the polarization resistances deriving from the electrodes. Therefore, the performance of the present MS–SOFCs has potentials for further improvement by optimizing the structure or material of the electrodes.

Stability of the MS–SOFC measured at 650 °C and 0.7 V is shown in Fig. 2.33 and no obvious degradation is found. Compared with the sustaining degradation shown in Fig. 2.15a, MS–SOFCs using infiltrated SDC–430L as the anode shows a much higher stability than that of the MS–SOFC using infiltrated Ni–430L as the anode. The stable output power shown in Fig. 2.33 confirms that the particle coarsening and metallic inter-diffusion issues have been well addressed by using SDC as the anode catalyst.

2.3.4 Investigation of Infiltrated Ni–SDC–430L Anodes and the MS–SOFCs

In this section, taking advantages of the high catalytic activity of infiltrated Ni–430L anodes and good stability of the SDC–430L anodes, a Ni–SDC–430L anode was developed. The weight ratio of SDC to Ni is chosen to be 8:2. We surmise that the excessive SDC ceramic phase can restrict the growth of the Ni particles and an enhanced stability would be obtained.

Figure 2.34a reveals the XRD patterns of the Ni–SDC infiltrated 430L anode as obtained. It is found that after treating at 600 °C for 2 h in a reducing atmosphere (5% H_2/95% N_2), pure phase of SDC can be obtained. For the low Ni loading and the main peak overlap of Ni and 430L, Ni phase is not obvious in the XRD patterns.

Figure 2.34b shows the polarization resistances of the infiltrated Ni–SDC–430L anode measured at 650–800 °C in 97% H_2–3% H_2O. The polarization resistances are 0.075, 0.081, 0.09, and 0.112 Ω cm^2 at 800, 750, 700 and 650 °C, respectively.

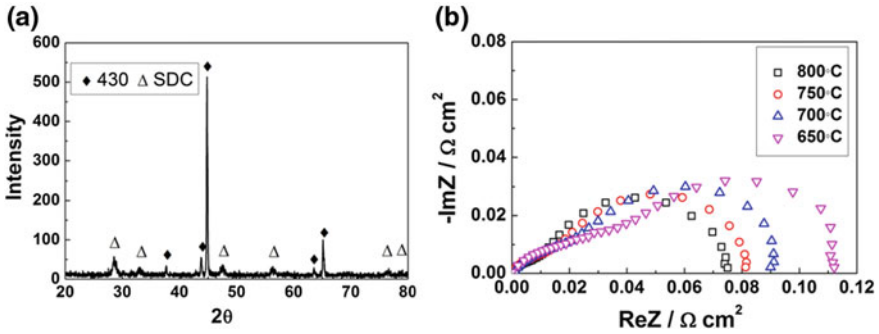


Fig. 2.34 **a** X-Ray diffraction patterns of the Ni–SDC–430L anode, **b** Impedance spectra of the symmetric Ni–SDC–430L anode cell. Reproduced with permission from Ref. [15]. Copyright 2014, The Electrochemical Society

Such results are comparable with a Ni–CGO infiltrated FeCr–YSZ cermet anode used in another MS–SOFC, which showed a polarization resistance of 0.12 Ω cm^2 at 650 °C [14]. It is interesting that the polarization resistances of the anode in this study change small with temperatures, corresponding to a low activation energy of 0.31 eV. The impedance spectra shown in Fig. 2.34b are composed of small high-frequency arcs and large low-frequency arcs at all temperatures ranging from 650 to 800 °C. It is reported that the high-frequency arc related to the charge transfer process near the TPB region is strongly dependent on temperature, while the low-frequency arc to the hydrogen dissociation adsorption or surface diffusion process on the anode surface is independent on temperature. Since the whole impedance spectra of the Ni–SDC–430L anode obtained here is dominated by the large low frequency arc (Fig. 2.34b), it is no wonder that the activation energy of the anode is very low. Above all, the low activation energy indicates that the Ni–SDC–430L anode is appropriate to be operated at low temperatures.

Compared with the SDC–430L anode, the Ni–SDC–430L anode obtained here shows a great decrease of the polarization resistance, especially at the lower temperatures (<700 °C) (Figs. 2.25 and 2.34b). A comparison of the Nyquist plots of the impedance data for the SDC–430L and the Ni–SDC–430L anode measured at 650 °C is shown in Fig. 2.35. The introduction of slight Ni into the SDC–430L anode can effectively reduce the polarization resistance from 0.230 to 0.112 Ω cm^2. As can be observed from Fig. 2.35, the reduction of the impedance is mainly centered at an intermediate frequency (5–400 Hz), which normally relates to a surface reaction [14].

The reaction pathways of the hydrogen oxidation reaction in the Ni–SDC–430L anode is schematically shown in Fig. 2.36. Similar to the SDC–430L anode, the 430L backbone acting as the electronic pathway while the SDC particles acting as both the ionic pathway and the reaction active sites. By adding Ni particles, TPBs of the SDC–430L anode are further enlarged from the surfaces of the SDC particles to the contacting areas between the SDC and Ni particles (marked in red in

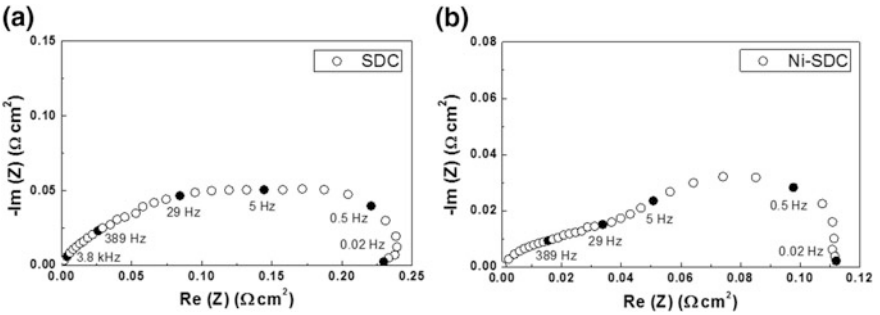


Fig. 2.35 Impedance spectra of the symmetrical anode cells: **a** SDC–430L, **b** Ni–SDC–430L

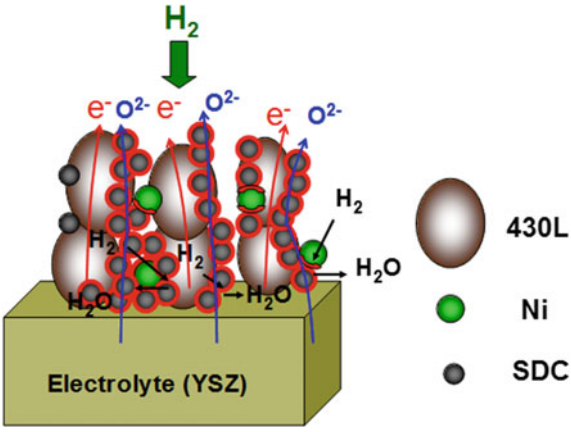


Fig. 2.36 Schematic diagram depicting the reaction pathways in Ni–SDC–430L anode

Fig. 2.36). Due to the higher catalytic activity of Ni than that of SDC, the hydrogen oxidation reaction of the SDC–430L anode is expected to be accelerated by adding Ni particles, which should be the reason to the fact that the Ni–SDC–430L anode has a much lower polarization resistance than that of the SDC–430L anode (Fig. 2.35) [14, 57].

Stability of the Ni–SDC–430L anode was also measured at 650 °C for 1200 h. As shown in Fig. 2.37a, an increase of polarization resistance from 0.12 to 0.3 Ω cm^2 is observed during the initial 500 h. After that, the polarization resistance is stabilized at around 0.3 Ω cm^2. Impedance spectra of the anode before and after the durability measurement are also shown in Fig. 2.37b. Consistent with the results of the infiltrated Ni–430L anode as shown above, the increase of the polarization resistance is mainly in the lower-frequency.

Figure 2.38 shows the SEM images of the Ni–SDC particles before and after the durability test. After the long-term test, coarsening of the particles and loss of the pores are shown. We surmise that the microstructure change would be the main reason for the increase of polarization resistance during the initial 500 h. While

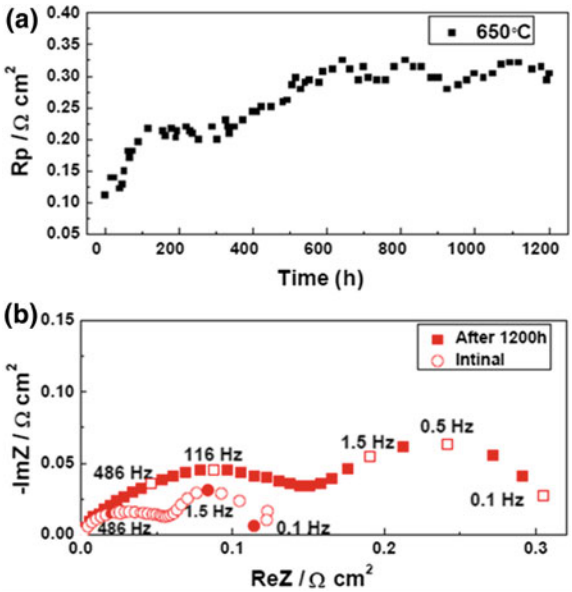


Fig. 2.37 **a** Stability of the polarization resistance for the Ni–SDC–430L anode, **b** Nyquist plots of the impedance data before and after the stability test. Reproduced with permission from Ref. [27]. Copyright 2014, Elsevier

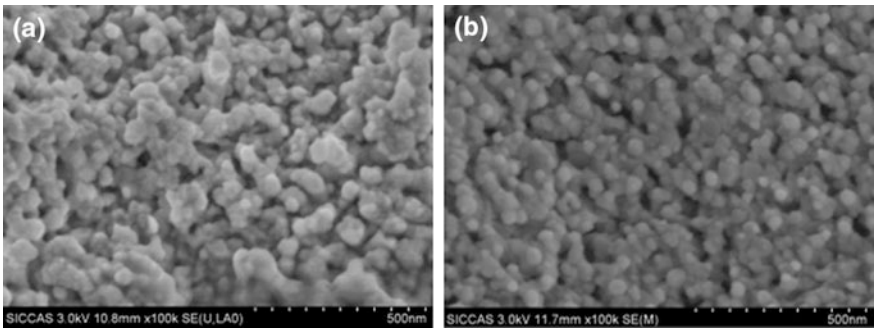


Fig. 2.38 Microstructures of the Ni–SDC particles: **a** Before and **b** After the stability test. Reproduced with permission from Ref. [27]. Copyright 2014, Elsevier

further extending the durability measurement may not change the microstructure and a stable polarization resistance is observed. We believe that if a pre-coarsening process is applied at the infiltrated Ni–SDC–430L anode as that at the Ni–430L anode, a stable polarization resistance can be obtained. Considering the low operation temperature, degradation mechanisms like metallic inter-diffusion between the

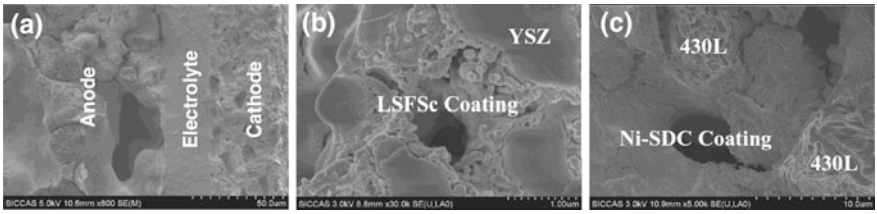


Fig. 2.39 SEM images of the: **a** MS–SOFC, **b** LSFSc–YSZ cathode, **c** Ni–SDC–430L anode. Reproduced with permission from Ref. [15]. Copyright 2014, The Electrochemical Society

supporting alloy substrates and the Ni anode catalysts and oxidation of the porous alloy substrates in humidified hydrogen may not be significant issues here.

Figure 2.39a shows a representative cross-sectional SEM micrograph of the single MS–SOFC, consisting of a porous Ni–SDC infiltrated 430L anode, a dense YSZ electrolyte and a porous LSFSc infiltrated YSZ cathode. The thickness of the cell component is about 40, 25 and 300 μm (part of the anode is not shown in this figure) for the cathode, electrolyte and anode, respectively. Well bonding between the electrolyte and the adjacent layers is presented clearly. Figure 2.39b and c show a high-magnification SEM micrograph of the LSFSc–YSZ cathode (30 wt% LSFSc loading) and Ni–SDC–430L anode (10 wt% Ni–SDC loading), respectively. Both the particle diameter and the pore size are ≈100 nm for the infiltrated LSFSc catalysts. While for the infiltrated Ni–SDC catalysts, the average particle diameter is ≈20–50 nm and the mean pore size is ≈50 nm.

Typical cell voltages and power densities of the MS–SOFC are shown in Fig. 2.40a as functions of current densities. The open circuit voltages decrease from 1.12 V at 600 °C to 1.07 V at 800 °C and are within 50 mV of the thermodynamically expected Nernst potentials, indicating excellent impermeability of the YSZ electrolyte shown in Fig. 2.39a. The MPDs are 0.4, 0.68, 0.92, 1.09 and

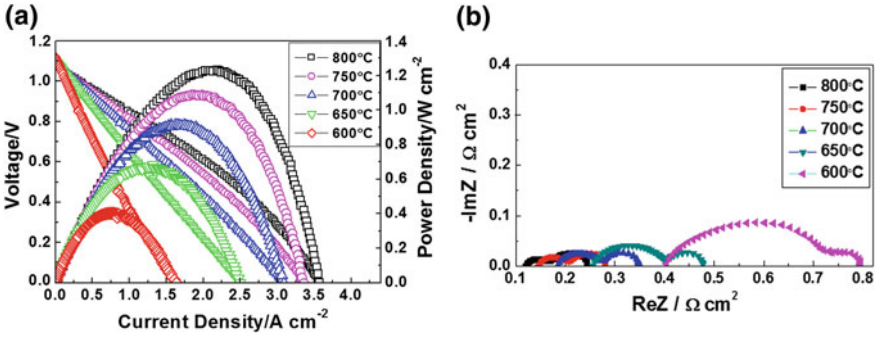


Fig. 2.40 Electrochemical characteristics of the single cell measured at 600–800 °C: **a** I–P–V characteristics, **b** Impedance spectra. Reproduced with permission from Ref. [15]. Copyright 2014, The Electrochemical Society

1.23 W cm^{-2} at 600, 650, 700, 750 and 800 °C, respectively. Compared with those of the MS–SOFCs using infiltrated Ni or SDC as the anodes, the power densities represented here show a significant improvement, especially at low temperatures. Considering the 25 μm thick YSZ electrolyte applied here, the maximum power output of 0.4 W cm^{-2} at 600 °C is encouraging. Such performances are even comparable with other MS–SOFCs using SDC as the electrolytes [58–60]. Since the oxide ion conductivity of the YSZ electrolyte used in this study is lower than that of the SDC electrolyte, the high cell performance at low temperature of 600 °C may be attributed to the nano-structured electrode catalysts. Figure 2.40b shows the Nyquist plots of the impedance data obtained at open circuits for the present MS–SOFCs. The pure ohmic resistances are 0.12, 0.15, 0.19 and 0.26 Ω cm^2 and the combined interfacial polarization resistances are 0.12, 0.13, 0.16 and 0.22 Ω cm^2 at 800, 750, 700 and 650 °C, respectively. In contrast to the MS–SOFCs using infiltrated Ni or SDC as the anode whose resistances were dominated by the polarization part, the ohmic and the polarization resistance play a comparable role in the cell using Ni–SDC as the anode.

Short-term stabilities of the single MS–SOFC with a cell configuration of "Ni–SDC infiltrated 430L anode/scandia-stabilized zirconia (SSZ) electrolyte/LSFSc infiltrated SSZ cathode" measured at 700–600 °C are shown in Fig. 2.41. SSZ was applied here due to its higher oxide ionic conductivity than that of YSZ, especially at lower temperatures (<700 °C). As shown in Fig. 2.41a, a rapid voltage decrease (from 0.804 to 0.645 V) is found when measured at 700 °C with a current density of 0.86 A cm^{-2}. Note that reducing the operating temperature and current density exhibit a more stable performance. As shown in Fig. 2.41b, a slight decrease of voltage from 0.70 to 0.694 V is observed during the 357 h measurement at 650 °C and 0.57 A cm^{-2}. No degradation is found when further reducing the operating temperature to 600 °C and current density to 0.4 A cm^{-2} (Fig. 2.41c).

I–V–P characteristics of the MS–SOFC measured after the 0, 80 and 175 h operation at 700 °C is shown in Fig. 2.42a. A decrease of MPD from 0.72 to 0.62 W cm^{-2} is found during the 80 h operation. The continued operation caused a gradual degradation, e.g., a MPD of 0.55 W cm^{-2} is obtained when measured after the 175 h operation. Nyquist plots of the impedance data obtained before and after

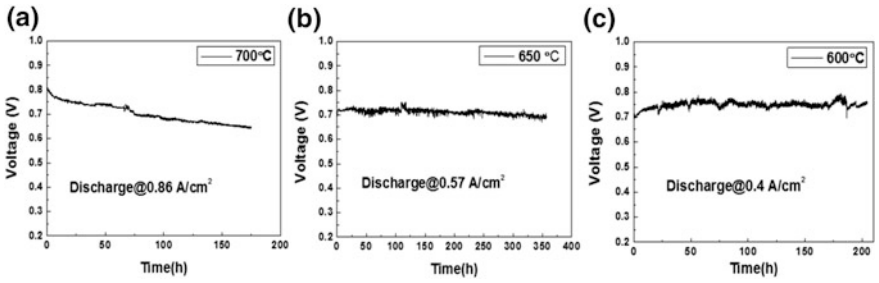


Fig. 2.41 Stability of the MS–SOFC measured at: **a** 700 °C, **b** 650 °C, **c** 600 °C. Reproduced with permission from Ref. [61]. Copyright 2015, Elsevier

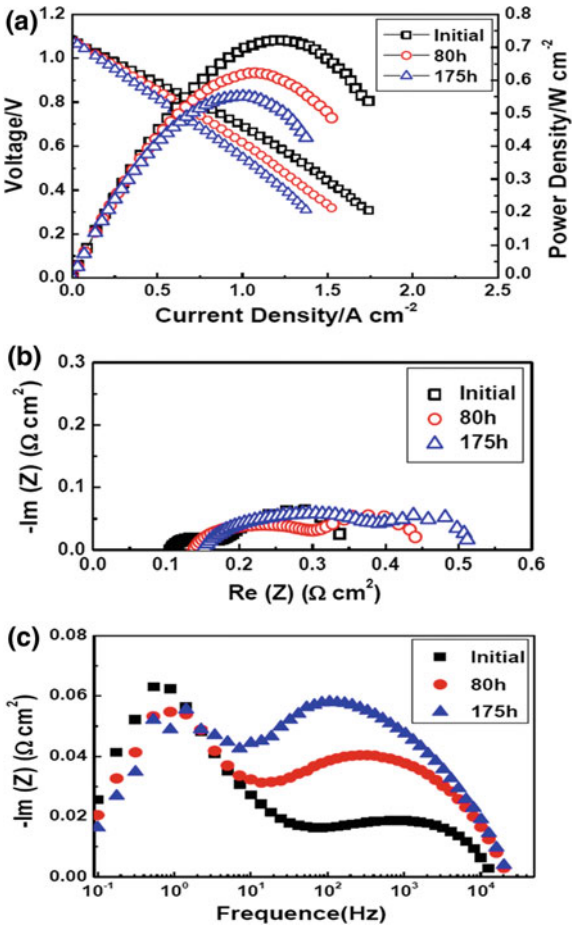


Fig. 2.42 Electrochemical characteristics of the MS–SOFC before and after the stability test measured at 700 °C: **a** I–P–V characteristics, **b** Nyquist plots of the impedance spectra, **c** Bode plots of the impedance spectra. Reproduced with permission from Ref. [61]. Copyright 2015, Elsevier

the stability test are shown in Fig. 2.42b. During the 175 h stability test, the pure ohmic resistance (*Ro*) increases from 0.10 to 0.15 Ω cm^2 while the polarization resistance (*Rp*) changes from 0.24 to 0.36 Ω cm^2. Since the *Ro* mainly derives from the ohmic resistances of the electrolyte/electrodes and the interfaces between different layers, the increase of the *Ro* maybe caused by the oxidation of the 430L substrate in the humidified hydrogen and/or the reduced adhesion between the 430L support and the electrolyte [62, 63]. From Bode plots of the EIS collected at OCV before and after the stability test (Fig. 2.42c), it is observed that the Rp change is characterized by the increased impedance at intermediate frequencies between 100 Hz and 10 kHz. As reported, for the Ni:CGO infiltrated cermet anode, the high frequency impedance arc was attributed to the oxide ion charge transfer resistance between the electrolyte and the infiltrated anode (summit frequency around 500 kHz), the intermediate frequency arc (summit frequency around 300 Hz) was ascribed to the electrochemistry of the electrode reaction, while the low frequency

arc (summit frequency around 4 Hz) was shown to be related to the gas composition. Since the infiltrated particles are easy to be coarsened, we surmise that the micrographs change of the cell electrodes which would decrease the active surface area should be the main reason to the increase of the polarization resistance.

To verify the surmise above, SEM micrographs of the Ni–SDC infiltrated 430L anodes and LSFSc infiltrated SSZ cathodes before and after the durability tests were examined. As shown in Fig. 2.43a–d, coarsening of the particles and cracking of the infiltrated coatings are clearly observed for the anodes measured after the stability tests carried out at a temperature range of 600–700 °C. In contrast, no obvious changes in the morphologies of the LSFSc infiltrated SSZ cathodes are observed before and after the stability tests (Fig. 2.44a–d). This is consistent with our previous report which showed that no pronounced changes both in LSFSc particle size and morphology were observed after the 400 h durability test measured at 650 °C (Fig. 2.16) [31]. Based on the SEM results shown in Fig. 2.43, we can conclude that morphological change of the infiltrated Ni–SDC coating reducing the TPB length should be the main reason to the cell performance degradation. Previous work showed that higher operation temperatures and higher current densities could accelerate the coarsening of the electrodes [64–66]. That should be the reason why the morphological change was particularly serious for the anode tested at 700 °C and 0.86 A cm^{-2} (Fig. 2.43b).

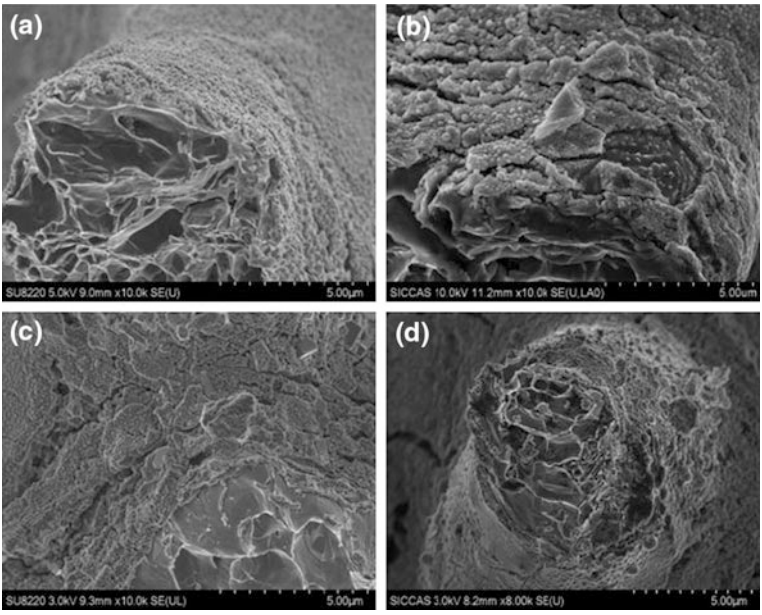


Fig. 2.43 SEM images of the Ni–SDC–430L anodes: **a** Before the stability test and after the stability test measured at **b** 700 °C, **c** 650 °C, **d** 600 °C. Reproduced with permission from Ref. [61]. Copyright 2015, Elsevier

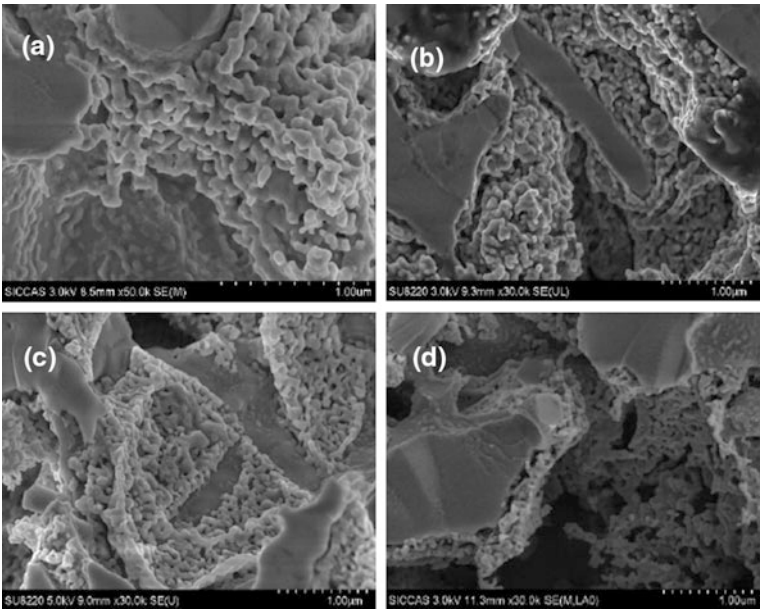
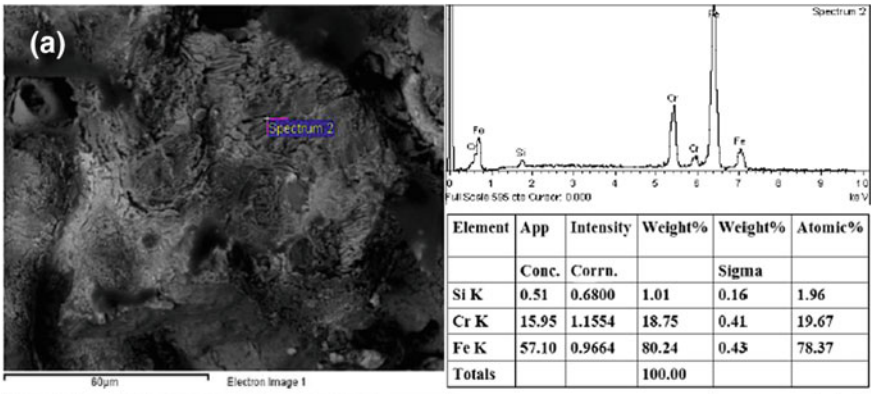


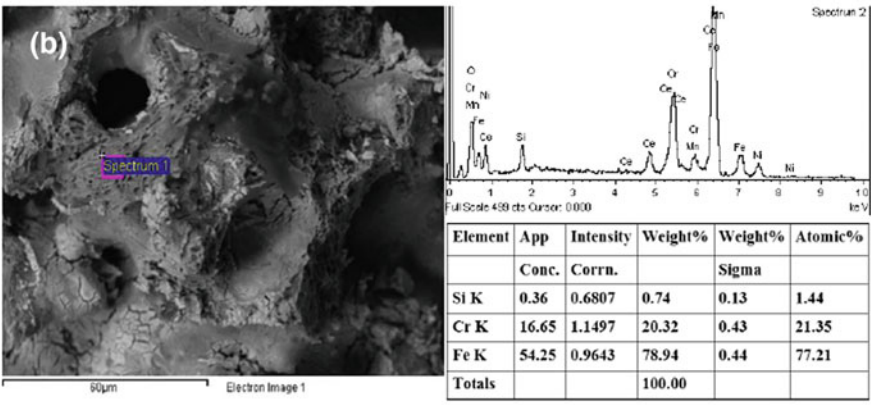
Fig. 2.44 SEM images of the LSFSc–SSZ cathodes: **a** Before the stability test and after the stability test measured at **b** 700 °C, **c** 650 °C, **d** 600 °C. Reproduced with permission from Ref. [61]. Copyright 2015, Elsevier

In order to identify whether inter-diffusions of Fe, Ni and Cr occurred in this study, energy dispersive X-ray spectroscopy (EDS) spectrums of the 430L backbones before and after the stability tests were measured (Fig. 2.45). All of the samples reflect the compositions of Fe–Cr and no Ni element is detected. It suggests that the metal element diffusion issue may not be the problem here.

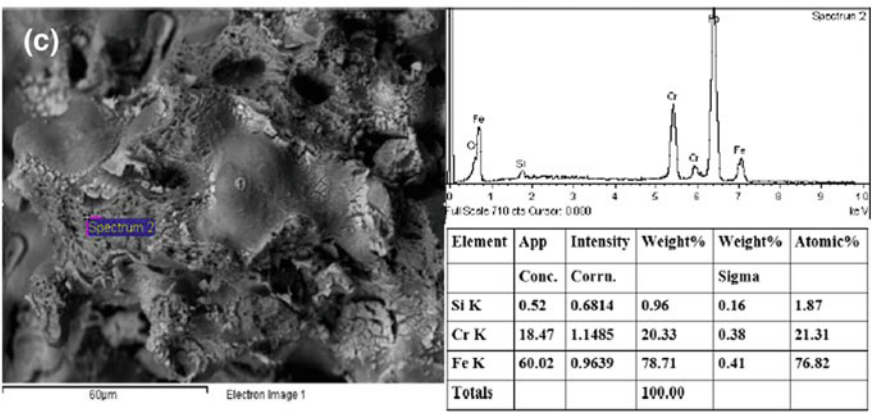
Since both the temperature and the current load are varied in Fig. 2.41, it is hard to identify the impact of current density and temperature on degradation independently. Stabilities of the MS–SOFC measured at varied current densities and temperatures were further studied and shown in Fig. 2.46. To evaluate the impact of current density on degradation, we kept the temperature constant. As shown in Fig. 2.46, the degradation rate is 9.23% (from 0.802 to 0.728 V) when measured at 700 °C and 0.86 A cm^{-2}, while a much higher degradation rate of 15.57% (from 0.501 to 0.423 V) is found when the fuel cell operated under a higher current density of 1.23 A cm^{-2}. Furthermore, to evaluate the impact of temperature on degradation, the applied current densities were kept similar (0.86 A cm^{-2} at 700 °C and 0.90 A cm^{-2} at 650 °C). It is found that the degradation rate are 9.23% (from 0.802 to 0.728 V) and 2.61% (from 0.537 to 0.523 V) when measured at 700 °C and 650 °C, respectively. In conclusion, both the current density and temperature have great impact on the stability of the MS–SOFC and larger current densities and higher temperatures would cause more significant degradation.



Element	App	Intensity	Weight%	Weight%	Atomic%
	Conc.	Corrn.		Sigma	
Si K	0.51	0.6800	1.01	0.16	1.96
Cr K	15.95	1.1554	18.75	0.41	19.67
Fe K	57.10	0.9664	80.24	0.43	78.37
Totals			100.00		

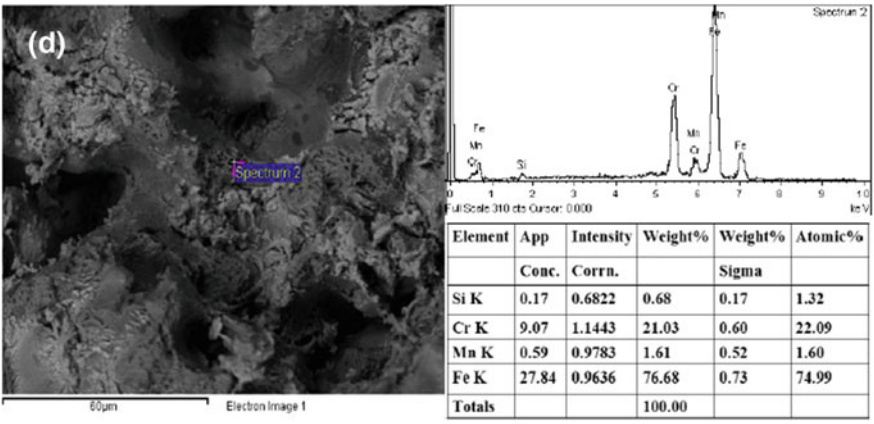


Element	App	Intensity	Weight%	Weight%	Atomic%
	Conc.	Corrn.		Sigma	
Si K	0.36	0.6807	0.74	0.13	1.44
Cr K	16.65	1.1497	20.32	0.43	21.35
Fe K	54.25	0.9643	78.94	0.44	77.21
Totals			100.00		



Element	App	Intensity	Weight%	Weight%	Atomic%
	Conc.	Corrn.		Sigma	
Si K	0.52	0.6814	0.96	0.16	1.87
Cr K	18.47	1.1485	20.33	0.38	21.31
Fe K	60.02	0.9639	78.71	0.41	76.82
Totals			100.00		

Fig. 2.45 EDS spectra of the 430L backbone: **a** Before the stability test and after the stability test measured at **b** 700 °C, **c** 650 °C, **d** 600 °C. Reproduced with permission from Ref. [61]. Copyright 2015, Elsevier



Element	App Conc.	Intensity Corrn.	Weight%	Weight% Sigma	Atomic%
Si K	0.17	0.6822	0.68	0.17	1.32
Cr K	9.07	1.1443	21.03	0.60	22.09
Mn K	0.59	0.9783	1.61	0.52	1.60
Fe K	27.84	0.9636	76.68	0.73	74.99
Totals			100.00		

Fig. 2.45 (continued)

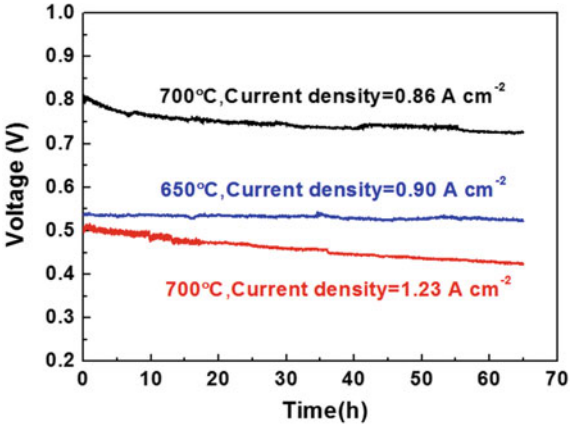


Fig. 2.46 Stabilities of the MS–SOFC measured at varied current densities and temperatures. Reproduced with permission from Ref. [61]. Copyright 2015, Elsevier

Long-term stability of the single cell operated at 650 °C under a high current density of 0.9 A cm^{-2} is shown in Fig. 2.47. Voltage decrease is found in the initial 500 h while no obvious change is found during the subsequent 1000 h measurement. It is consistent with the durability test of the Ni–SDC infiltrated 430L anode, which showed that the polarization resistance of the anode increases from 0.12 to 0.3 Ω cm^2 during the initial 500 h while no degradation is found during the subsequent measurement at 650°C [27]. This result further confirms our conclusion that the cell degradation is caused by the anode. As shown in Fig. 2.47, during the 1500 h measurement, a degradation rate of 1.3% kh^{-1} in cell voltage is found. Another MS–SOFC with a FeCr alloy support, CGO–Ni infiltrated cermet anode, ScYSZ electrolyte and LSCF cathode exhibited a more stable performance, i.e.,

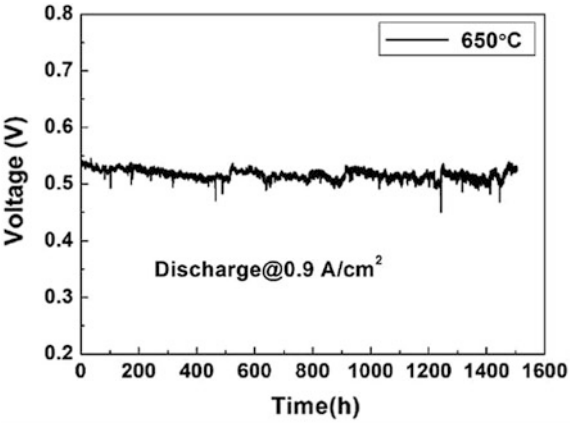


Fig. 2.47 Long-term stability of the MS–SOFC measured at 650 °C. Reproduced with permission from Ref. [61]. Copyright 2015, Elsevier

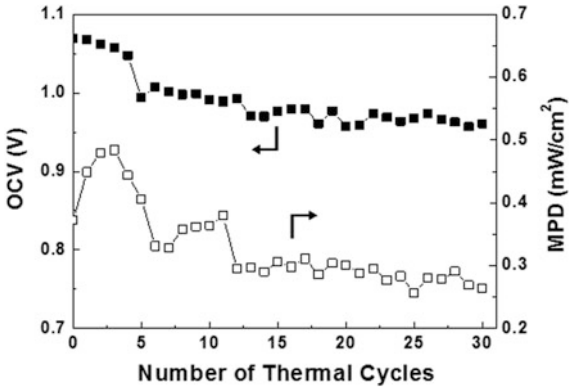


Fig. 2.48 OCV and MPD retention of the MS–SOFCs upon 30 thermal cycles

0.9% kh^{-1} at 650 °C [34]. The differences in cell durability may be caused by the different current densities, e.g., current load of 0.9 A cm^{-2} was applied here while it was only 0.25 A cm^{-2} in that report.

In this study, the thermal shock resistance of the MS–SOFCs was investigated between 100 and 650 °C at a rate of 10 °C min^{-1}. Figure 2.48 shows the OCV and MPD retention of the MS–SOFCs upon 30 thermal cycles. Both of the OCV and MPD show a continuous degradation during the initial 11 cycles and then tend to be stable during the following cycles. Figure 2.49 shows the decrease of the OCV and increase of the ohmic resistance which should be caused by the thermal stress. Thermal shock resistance of the MS–SOFCs should be further improved by optimizing the cell structure and materials.

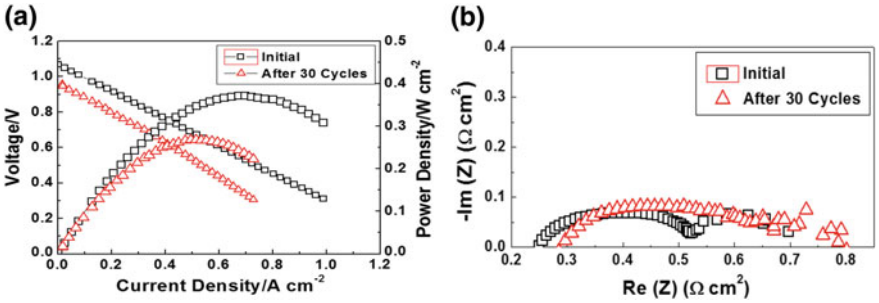


Fig. 2.49 Electrochemical characteristics of the MS–SOFC before and after the thermal cycles: **a** I–P–V characteristics, **b** Impedance spectra

2.4 Conclusions

In this chapter, intermediate-temperature MS–SOFCs based on the structure of "porous Ni/SDC/Ni–SDC infiltrated 430L anode | dense YSZ/SSZ electrolyte | porous LSFSc infiltrated YSZ/SSZ cathode" were developed. The structure-performance relationship of the electrodes, reaction kinetics of the electrodes and degradation mechanism of the single cells were also investigated. The specific conclusions are listed as follows:

1. LSFSc cathode and Ni-based anode materials were applied by the infiltration method to reduce the polarization resistances of the cathode and anode, respectively. When measured at 650 °C, polarization resistances of the infiltrated LSFSc–YSZ cathode, Ni–430L anode, SDC–430L anode and Ni–SDC–430L anode were 0.160, 2.2, 0.233 and 0.112 Ω cm^2, respectively.
2. Coarsening of the Ni particles and elemental inter-diffusion between Ni and 430L would cause the degradation of the Ni–430L anode.
3. Kinetic studies indicated that the low frequency peak of the impedance spectra of the SDC–430L anode was associated with the extraction of surface lattice oxygen of SDC while the high frequency peak was attributed to the transport of oxide-ions within the SDC coating.
4. MPD of the MS–SOFC with Ni–SDC–430L anode were 1.23, 0.92 and 0.40 W cm^{-2} when measured at 800, 700 and 600 °C, respectively. A degradation rate of 1.3% kh^{-1} was shown when measured at 650 °C for 1500 h. The degradation rate was faster at higher operation temperatures and larger current densities and the degradation was mainly caused by the morphological change of the anode.

References

1. Tucker MC (2010) Progress in metal-supported solid oxide fuel cells: a review. J Power Sources 195:4570–4582
2. Tucker MC, Lau GY, Jacobson CP, DeJonghe LC, Visco SJ (2008) Stability and robustness of metal-supported SOFCs. J Power Sources 175:447–451
3. Leah RT, Brandon NP, Aguiar P (2005) Modelling of cells, stacks and systems based around metal-supported planar IT-SOFC cells with CGO electrolytes operating at 500–600 °C. J Power Sources 145:336–352
4. Brandner M, Bram M, Froitzheim J, Buchkremer HP, Stoever D (2008) Electrically conductive diffusion barrier layers for metal-supported SOFC. Solid State Ionics 179:1501–1504
5. Franco T, Schibinger K, Ilhan Z, Schiller G, Venskutonis A (2007) Ceramic diffusion barrier layers for metal supported SOFCs. In: Eguchi K, Singhai SC, Yokokawa H, Mizusaki H (eds) Solid oxide fuel cells, vol 10, pp 771–780
6. Hwang C, Tsai C-H, Lo C-H, Sun C-H (2008) Plasma sprayed metal supported YSZ/Ni–LSGM–LSCF ITSOFC with nanostructured anode. J Power Sources 180:132–142
7. Ishihara T, Yan J, Enoki M, Okada S, Matsumoto H (2008) Ni-Fe alloy-supported intermediate temperature SOFCs using $LaGaO_3$ electrolyte film for quick startup. J Fuel Cell Sci Technol 5:031205
8. Nedelec R, Neagu R, Uhlenbruck S, Maric R, Sebold D, Buchkremer HP et al (2011) Gas phase deposition of diffusion barriers for metal substrates in solid oxide fuel cells. Surf Coat Technol 205:3999–4004
9. Ju Y-W, Hong J-E, Hyodo J, Inagaki T, Ida S, Ishihara T (2012) New buffer layer material La(Pr)CrO_3 for intermediate temperature solid oxide fuel cell using $LaGaO_3$-based electrolyte film. J Mater Res 27:1906–1914
10. Hui R, Berghaus JO, Deces-Petit C, Qu W, Yick S, Legoux J-G et al (2009) High performance metal-supported solid oxide fuel cells fabricated by thermal spray. J Power Sources 191:371–376
11. Yoo Y, Wang Y, Deng X, Singh D, Legoux J-G (2012) Metal supported tubular solid oxide fuel cells fabricated by suspension plasma spray and suspension high velocity oxy-fuel spray. J Power Sources 215:307–311
12. Vohs JM, Gorte RJ (2009) High-performance SOFC cathodes prepared by infiltration. Adv Mater 21:943–956
13. Blennow P, Hjelm J, Klemenso T, Ramousse S, Kromp A, Leonide A et al (2011) Manufacturing and characterization of metal-supported solid oxide fuel cells. J Power Sources 196:7117–7125
14. Blennow P, Hjelm J, Klemenso T, Persson AH, Ramousse S, Mogensen M (2011) Planar metal-supported SOFC with novel cermet anode. Fuel Cells 11:661–668
15. Zhou Y, Ye X, Li J, Zhan Z, Wang S (2014) Metal-supported solid oxide fuel cells with a simple structure. J Electrochem Soc 161:F332–F336
16. Chen J, Liang FL, Liu LN, Jiang SP, Chi B, Pu J et al (2008) Nano-structured (La, Sr)(Co, Fe)O_3 + YSZ composite cathodes for intermediate temperature solid oxide fuel cells. J Power Sources 183:586–589
17. Huang Y, Vohs JM, Gorte RJ (2004) Fabrication of Sr-doped $LaFeO_3$ YSZ composite cathodes. J Electrochem Soc 151:A646–A651
18. Zhang Y, Sun Q, Xia C, Ni M (2013) Geometric properties of nanostructured solid oxide fuel cell electrodes. J Electrochem Soc 160:F278–F289
19. Sholklapper TZ, Kurokawa H, Jacobson C, Visco S, De Jonghe L (2007) Nanostructured solid oxide fuel cell electrodes. Nano Lett 7:2136–2141
20. Siebert E, Hammouche A, Kleitz M (1995) Impedance spectroscopy analysis of $La_{1-x}Sr_xMnO_3$-yttria-stabilized zirconia electrode kinetics. Electrochim Acta 40:1741–1753

21. Tsuneyoshi K, Mori K, Sawata A, Mizusaki J, Tagawa H (1989) Kinetic studies on the reaction at the $La_{0.6}Ca_{0.4}MnO_3$/YSZ interface, as an SOFC air electrode. Solid State Ionics 35:263–268
22. Takeda Y, Kanno R, Noda M, Tomida Y, Yamamoto O (1987) Cathodic polarization phenomena of perovskite oxide electrodes with stabilized zirconia. J Electrochem Soc 134:2656–2661
23. Escudero MJ, Aguadero A, Alonso JA, Daza L (2007) A kinetic study of oxygen reduction reaction on La_2NiO_4 cathodes by means of impedance spectroscopy. J Electroanal Chem 611:107–116
24. Wang Y, Zhang L, Chen F, Xia C (2012) Effects of doped ceria conductivity on the performance of $La_{0.6}Sr_{0.4}Co_{0.2}Fe_{0.8}O_{3-\delta}$ cathode for solid oxide fuel cell. Int J Hydrogen Energy 37:8582–8591
25. Kim JD, Kim GD, Moon JW, Park YI, Lee WH, Kobayashi K et al (2001) Characterization of LSM-YSZ composite electrode by ac impedance spectroscopy. Solid State Ionics 143:379–389
26. Li Q, Xia T, Sun L, Zhao H, Huo L (2014) Electrochemical performance of novel cobalt-free perovskite $SrFe_{0.7}Cu_{0.3}O_{3-\delta}$ cathode for intermediate temperature solid oxide fuel cells. Electrochim Acta 150:151–156
27. Zhou Y, Yuan C, Chen T, Meng X, Ye X, Li J et al (2014) Evaluation of Ni and Ni–$Ce_{0.8}Sm_{0.2}O_{2-\delta}$ (SDC) impregnated 430L anodes for metal-supported solid oxide fuel cells. J Power Sources 267:117–122
28. Liu X, Meng X, Han D, Wu H, Zeng F, Zhan Z (2013) Impregnated nickel anodes for reduced-temperature solid oxide fuel cells based on thin electrolytes of doped $LaGaO_3$. J Power Sources 222:92–96
29. Chen M, Kim BH, Xu Q, Ahn BG, Huang DP (2010) Effect of Ni content on the microstructure and electrochemical properties of Ni–SDC anodes for IT-SOFC. Solid State Ionics 181:1119–1124
30. Jiang S, Badwal S (1999) An electrode kinetics study of H_2 oxidation on Ni/Y_2O_3-ZrO_2 cermet electrode of the solid oxide fuel cell. Solid State Ionics 123:209–224
31. Zhou Y, Xin X, Li J, Ye X, Xia C, Wang S et al (2014) Performance and degradation of metal-supported solid oxide fuel cells with impregnated electrodes. Int J Hydrogen Energy 39:2279–2285
32. Ansar A, Szabo P, Arnold J, Ilhan Z, Soysal D, Costa R et al (2011) Metal supported solid oxide fuel cells and stacks for auxiliary power units—progress, challenges and lessons learned. Solid Oxide Fuel Cells 12 (Sofc Xii). 35:147–55
33. Soysal D, Ansar A, Ilhan Z, Costa R (2011) Nanostructured composite cathodes by suspension plasma spraying for SOFC applications. In: Singhal SC, Eguchi K (eds) Solid oxide fuel cells, vol 12, pp 2233–2241
34. Klemenso T, Nielsen J, Blennow P, Persson AH, Stegk T, Christensen BH et al (2011) High performance metal-supported solid oxide fuel cells with Gd-doped ceria barrier layers. J Power Sources 196:9459–9466
35. Simner SP, Shelton JP, Anderson MD, Stevenson JW (2003) Interaction between La (Sr) FeO_3 SOFC cathode and YSZ electrolyte. Solid State Ionics 161:11–18
36. Liu Y, Chen K, Zhao L, Chi B, Pu J, Jiang SP et al (2014) Performance stability and degradation mechanism of $La_{0.6}Sr_{0.4}Co_{0.2}Fe_{0.8}O_{3-\delta}$ cathodes under solid oxide fuel cells operation conditions. Int J Hydrogen Energy 39:15868–15876
37. Hathiramani D, Vaßen R, Mertens J, Sebold D, Haanappel VAC, Stöver D (2008) Degradation mechanism of metal supported atmospheric plasma sprayed solid oxide fuel cells. In: Advances in solid oxide fuel cells II: ceramic engineering and science proceedings. Wiley, New York, pp 55–65
38. Franco T, HoshiarDin Z, Szabo P, Lang M, Schiller G (2007) Plasma sprayed diffusion barrier layers based on doped perovskite-type $LaCrO_3$ at substrate-anode interface in solid oxide fuel cells. J Fuel Cell Sci Technol 4:406–412

39. Choi JH, Lee T, Choi M, Yoo Y-S, Baek S-W, Bae J (2010) Long-term performance of anode-supported SOFC integrated with metal interconnect by joining process. Int J Hydrogen Energy 35:4285–4291
40. Shaigan N, Qu W, Ivey DG, Chen W (2010) A review of recent progress in coatings, surface modifications and alloy developments for solid oxide fuel cell ferritic stainless steel interconnects. J Power Sources 195:1529–1542
41. Fergus JW (2005) Metallic interconnects for solid oxide fuel cells. Mater Sci Eng A 397: 271–283
42. Molin S, Kusz B, Gazda M, Jasinski P (2008) Evaluation of porous 430L stainless steel for SOFC operation at intermediate temperatures. J Power Sources 181:31–37
43. Lee JG, Park JH, Shul YG (2014) Tailoring gadolinium-doped ceria-based solid oxide fuel cells to achieve 2 W cm^{-2} at 550 °C. Nat Commun 5:4045
44. Ding C, Hashida T (2010) High performance anode-supported solid oxide fuel cell based on thin-film electrolyte and nanostructured cathode. Energy Environ Sci 3:1729–1731
45. Chen Y, Liu Q, Yang Z, Chen F, Han M (2012) High performance low temperature solid oxide fuel cells with novel electrode architecture. RSC Adv 2:12118–12121
46. Xia C, Liu M (2001) Low-temperature SOFCs based on $Gd_{0.1}Ce_{0.9}O_{1.95}$ fabricated by dry pressing. Solid State Ionics 144:249–255
47. Désaunay T, Bonura G, Chiodo V, Freni S, Couzinié JP, Bourgon J et al (2013) Surface-dependent oxidation of H_2 on CeO_2 surfaces. J Catal 297:193–201
48. Chen B, Ma Y, Ding L, Xu L, Wu Z, Yuan Q et al (2013) Reactivity of hydroxyls and water on a CeO_2 (111) thin film surface: the role of oxygen vacancy. J Phys Chem C 117: 5800–5810
49. Zhou Y, Luo T, Du X, Wang J, Yang W, Sun C et al (2014) High activity of nanoporous—$Sm_{0.2}Ce_{0.8}O_{2-\delta}$@ 430L composites for hydrogen electro—oxidation in solid oxide fuel cells. Adv Energy Mater 4:1400883
50. Hagen A, Liu YL, Barfod R, Hendriksen PV (2007) Anode supported solid oxide fuel cells—deconvolution of degradation into cathode and anode contributions. ECS Trans 7:301–309
51. Bastidas DM, Tao S, Irvine JTS (2006) A symmetrical solid oxide fuel cell demonstrating redox stable perovskite electrodes. J Mater Chem 16:1603–1605
52. Liu Q, Dong X, Xiao G, Zhao F, Chen F (2010) A novel electrode material for symmetrical SOFCs. Adv Mater 22:5478–5482
53. Gross MD, Vohs JM, Gorte RJ (2007) A strategy for achieving high performance with SOFC ceramic anodes. Electrochem Solid-State Lett 10:B65–B69
54. Alam MK, Ahmed F, Miura R, Suzuki A, Tsuboi H, Hatakeyama N et al (2011) Surface reduction processes of cerium oxide surfaces by H2 using ultra accelerated quantum chemical molecular dynamic study. Catal Today 164:9–15
55. Zhang C, Yu Y, Grass ME, Dejoie C, Ding W, Gaskell K et al (2013) Mechanistic studies of water electrolysis and hydrogen electro-oxidation on high temperature ceria-based solid oxide electrochemical cells. J Am Chem Soc 135:11572–11579
56. Souza ECC, Chueh WC, Jung W, Muccillo ENS, Haile SM (2012) Ionic and electronic conductivity of nanostructured, samaria-doped ceria. J Electrochem Soc 159:K127–K135
57. Nielsen J, Klemenso T, Blennow P (2012) Detailed impedance characterization of a well performing and durable Ni:CGO infiltrated cermet anode for metal-supported solid oxide fuel cells. J Power Sources 219:305–316
58. Xie Y, Neagu R, Hsu C-S, Zhang X, Deces-Petit C, Qu W et al (2010) Thin film solid oxide fuel cells deposited by spray pyrolysis. J Fuel Cell Sci Technol 7:021007
59. Oberste Berghaus J, Legoux JG, Moreau C, Hui R, Deces-Petit C, Qu W et al (2008) Suspension HVOF spraying of reduced temperature solid oxide fuel cell electrolytes. J Therm Spray Technol 17:700–707
60. Oishi N, Yoo Y, Davidson I (2007) Fabrication of a metal-supported ceria cell by wet powder spray and its characterization at intermediate temperatures. ECS Trans 7:781–786

61. Zhou Y, Chen T, Li J, Yuan C, Xin X, Chen G et al (2015) Long-term stability of metal-supported solid oxide fuel cells employing infiltrated electrodes. J Power Sources 295:67–73
62. Knibbe R, Wang H-J, Blennow P, Thydén K, Persson ÅH, Mikkelsen L et al (2013) Oxidation in ceria infiltrated metal supported SOFCs—a TEM investigation. J Power Sources 228:75–82
63. Sarasketa-Zabala E, Otaegi L, Rodriguez-Martinez LM, Alvarez MA, Burgos N, Castro F et al (2012) High temperature stability of porous metal substrates under highly humidified hydrogen conditions for metal supported Solid Oxide Fuel Cells. Solid State Ionics 222:16–22
64. Meng X, Han D, Wu H, Li J, Zhan Z (2014) Characterization of $SrFe_{0.75}Mo_{0.25}O_{3-\delta}$–$La_{0.9}Sr_{0.1}Ga_{0.8}Mg_{0.2}O_{3-\delta}$ composite cathodes prepared by infiltration. J Power Sources 246:906–911
65. Komatsu T, Yoshida Y, Watanabe K, Chiba R, Taguchi H, Orui H et al (2010) Degradation behavior of anode-supported solid oxide fuel cell using LNF cathode as function of current load. J Power Sources 195:5601–5605
66. Hatae T, Matsuzaki Y, Yamashita S, Yamazaki Y (2009) Current density dependence of changes in the microstructure of SOFC anodes during electrochemical oxidation. Solid State Ionics 180:1305–1310

Springer

http://www.springer.com/978-981-10-6616-0

Study on Fabrication and Performance of Metal-Supported Solid Oxide Fuel Cells

Zhou, Y.

2018, XII, 93 p. 90 illus., Hardcover
ISBN: 978-981-10-6616-0